Journal of Materials Research and Technology 30 (2024) 3622–3639

Contents lists available at ScienceDirect

Journal of Materials Research and Technology

journal homepage: www.elsevier.com/locate/jmrt

Miniaturised experimental simulation and combined modelling of open-die forging of Ti-6Al-4V titanium alloy

David Connolly [a,b,*], Mathieu Fabris [a], Giribaskar Sivaswamy [a], Salaheddin Rahimi [a], Vassili Vorontsov [b]

[a] Advanced Forming Research Centre (AFRC), University of Strathclyde, 85 Inchinnan Drive, Inchinnan, Renfrewshire, PA4 9LJ, UK
[b] Design Manufacture and Engineering Management (DMEM), University of Strathclyde, Glasgow, G1 1XJ, UK

ARTICLE INFO

Keywords:
Open-die forging
Ti-6Al-4V
Materials processing
Cogging
Globularisation

ABSTRACT

This study demonstrates the application of a new experimental technique for laboratory-scale simulation of the open-die forging process, known as cogging, an intermediate hot-working process necessary to design an optimised microstructure in the advanced engineering titanium alloy Ti-6Al-4V. Small test-bars of Ti-6Al-4V alloy were subjected to multi-directional cogging operations at elevated temperatures (950–1050 °C). The as-received material, prior to forging, underwent heat treatments to coarsen the initial grain structure, to better simulate the industrial-scale intermediate microstructure (*i.e.,* β recrystallised) and to help prove the capability of the set-up to achieve microstructure modification via globularisation (below β-transus), and recrystallisation (dynamic and static) and recovery mechanisms (above β-transus) within the cogged material. The influences of hot working parameters on deformation localisation, width of α platelets, and globularisation within the resulting microstructure variation have been investigated using light microscopy (LM), Vickers hardness (HV) testing, and electron backscatter diffraction (EBSD). The cogged Ti-6Al-4V alloy specimens underwent various microstructural evolution stages after hot forging, thus indicating successful application of the designed miniaturised open-die forging apparatus for high temperature experimentation and characterisation studies. This will be suitable for low-cost small-scale trials to determine the key process parameters affecting the onset of microstructure evolution during open-die forging (*e.g.,* ingot-to-billet conversion) of the Ti-6Al-4V alloy, prior to large-scale trials which are rather more expensive.

1. Introduction

Titanium alloy components play a critical role in the aerospace, energy, and electric vehicle industries due to their high strength-to-weight ratio [1], outstanding fracture resistance and fatigue properties, as well as compatibility with carbon fibre composites [2,3]. Ti-6Al-4V (wt.%), also known as Ti-64, is widely acknowledged as the most popular titanium alloy. This α + β titanium alloy accounts for around half of all titanium products used worldwide. Conventional manufacture of Ti-6Al-4V products requires a series of processing steps that include casting, open- and closed-die forging, and/or rolling of bulk feedstock materials [4]. Due to the anisotropic nature of the material, these processes often result in non-uniform microstructures, and hence properties, within the interior of the billets. As a consequence, approximately 70% of the processed material is machined away to leave behind only the desired microstructure for the final part. This is both costly and wasteful. Consequently, there is a widespread industry push to produce components with more homogeneous microstructures and evenly distributed properties while minimising material and energy waste.

The high-value manufacturing sector urgently needs novel tools that can objectively inform engineers on the most optimal processing route based on key criteria: cost, volume, energy consumption, resource use, and in-service properties. This need is evident for both state-of-the-art and emerging routes, such as FAST-forge [5], as well as for established open/closed-die forging processes.

The numbers of studies on emerging routes such as precision investment casting and additive manufacturing (AM) of titanium alloys have recently increased. These technologies offer advantages over forging in terms of material and energy usage, and higher speed of manufacture, as evidenced in the works of Liu et al. [6], Herzog et al. [7], and Huang et al. [8]. However, they still cannot produce the required mechanical properties for many structure-critical applications,

* Corresponding author. Advanced Forming Research Centre (AFRC), University of Strathclyde, 85 Inchinnan Drive, Inchinnan, Renfrewshire, PA4 9LJ, UK.
E-mail address: connolly.david1234@gmail.com (D. Connolly).

https://doi.org/10.1016/j.jmrt.2024.04.084
Received 16 October 2023; Received in revised form 1 April 2024; Accepted 10 April 2024
Available online 16 April 2024

such as aero-engine discs. One prevalent issue is that of porosity that is observed in many cast and AM parts, which makes them unsuitable for fatigue-sensitive applications. Therefore, there is emerging research interest in overcoming the efficiency limitations of conventional thermo-mechanical processing (TMP) routes by dynamically cross-referencing them against their digital representation. Such approaches seek to combine constitutive models, forging data, and materials characterisation to create fully coupled digital-twin platforms and are at the forefront of current development [9] of future forging technologies.

Controlling the grain size and phase morphology through TMP is the current state-of-the-art for achieving desired mechanical properties with enhanced resistance to different modes of in-service deformation and failure (*e.g.,* fatigue fracture). The resulting microstructural changes are attributable to several different mechanisms, such as globularisation, dynamic, metadynamic, and static recrystallisation, which are active during hot deformation of Ti-6Al-4V and are strongly dependent on the processing temperature (*i.e.,* above or below the β-transus).

Due to the costly, resource-intensive, and complex nature of conventional ingot-to-billet conversion processes, finite element (FE) and combined crystal plasticity finite element (CPFE) modelling, *e.g.,* the FE work presented in Roters et al.'s work [10], has emerged as a primary means of research of open die forging operations such as cogging and upsetting. Such models have been applied successfully to the study of nickel-based superalloys, *e.g.* Perez et al. [11], Souza et al. [12] as well as titanium alloys Souza et al. [13]. This work is the first exploration into phenomenology of Ti-6Al-4V under multidirectional loading at this scale, as laboratory tests following the ASTM E209-18 [14] standard have only ever captured kinetics of the upsetting thermomechanical process.

There has also been significant attention given to the development of microstructure evolution models in order to predict the grain size distributions in components and billets produced by uni-directional (upsetting) and multi-directional (cogging) open die forging: *e.g.,* 3D thermo-plastic finite element analysis by Cho et al. [15], numerical models of cogging by Kukuryk et al. [16], microstructural evolution simulation during hot forging of Waspaloy by Kang et al. [17], and Bai et al.'s study on modelling the dominant softening mechanisms in Ti-6Al-4V during hot forming [18]. However, the validation of such models and their relevance to industrial manufacturing poses a practical challenge due to the sheer size and cost of many industrial billets, which, in many cases, cannot be sacrificed for the purposes of destructive microstructural characterisation. This factor has been considerably limiting in the availability of detailed microstructural studies of ingot-to-billet conversion of high-performance engineering alloys.

Nonetheless, there have been some noteworthy efforts in characterising the phenomenology of microstructure evolution during ingot-to-billet conversion with respect to the function of the process variables: forging temperature, strain rate, initial grain size, and the extent of plastic deformation. Examples of studies which used material sectioned from commercial triple-melted ingots include the works of Ding et al. [19] in Ti-6Al-4V and Coyne-Grell et al. [20,21] in superalloy AD730. The latter studies used material cut from the ends of the ingot that is normally removed during the manufacturing process. The aforementioned works have, however, only investigated unidirectional compression of the test specimens, which does not fully capture the effects of multi-directional deformation during the industrial process.

Zhang et al. [22] studied the effects of multi-directional isothermal forging on achieving grain refinement and enhanced mechanical properties in Ti-6Al-4V alloy, which was successful in achieving α-globularisation and fragmentation of the β phase, resulting in remarkable grain refinement. The study was limited to just three deformation steps/bites and the test-specimens came from a forged alloy bar and were subjected to super-transus homogenisation and quenching prior to forging. Nevertheless, the aforementioned works highlight the potential of reduced-scale experimental approaches for bettering our understanding of the microstructural transformation phenomena that occur during industrial ingot-to-billet conversion.

As investments in "close-to-industry scale" experimentation increase (*e.g.,* the ATI** funded Future Forge project) which is corroborated in works of Ward et al. [23], Rahimi et al. [24], and Blackwell et al. [25], it becomes essential to ensure the equivalence, relevance, and applicability of the results to industrially manufactured materials. Effective identification of trends in thermo-mechanical processing variables and insights to their effect on the microstructural evolution (and how they compare to the industrial scale) can be achieved through novel multi-directional open-die forging experiments, but requires a large number of tests to be carried out. Thus, there is a need for lower cost, higher throughput experimental techniques, which can inform (at least in part) larger scale testing and industrial manufacture. A comprehensive understanding of size and loading effects related to billet geometries, plastic strain levels, grain refinement, and microstructural evolution is crucial for the effective use of reduced-scale experimental methods for this purpose.

Titanium alloy TMP (following extraction, sponge generation, and melting processes) refers to a set of sequential hot working and heat treatment stages that are performed to transform the as-cast ingots into final shape products. Two distinct steps at this stage are: (i) primary working to convert ingots into mill products such as billets, flat rolled products, or bars [26], and (ii) secondary working that involves forging (*i.e.,* ring rolling, extrusion, or closed-die forging) and heat treatments (*i.e.,* to relieve residual stresses or improve strength) during which a desired shape for the final product is obtained. The primary working for titanium alloys, which is the focus in this work, is also split into 3 stages: (i) β hot working, (ii) initial α/β hot working with β recrystallisation heat treatment, and (iii) final α/β hot working.

This study builds on previous work detailing laboratory-scale cogging apparatus design and its effectiveness in achieving desired microstructure evolution (*e.g.,* grain-refinement) in a single-phase alloy [27]. It successfully demonstrates the capability of the said apparatus and experimental technique to control the microstructural evolution in alloys of high research and commercial interest. Specifically, the capability of hot forging titanium alloys was investigated. This requirement guided a number of additional design decisions with regard to the load frame capacity, specimen size with respect to available furnace volume, as well as the choice and geometry of tooling materials. Among the tests carried out, was the breakdown of intermediate β recrystallised material with lamellar structure to a globularised α microstructure, which is an industrially important microstructural optimisation explored in the works of Semiatin et al. [28], Souza et al. [29], and Sabban et al. [30]. Globularisation of the α -phase originates from strain localisation on the grain boundaries of deformed α lamellae within an α + β structure. This localised strain causes a build-up of micro-defects, *i.e.,* sub-boundary dislocations, which then creates a channel of dislocations for solute diffusion which can generate thermal interface grooving in the α platelet/lamellae which leads to globularised α grains, which is described and visualised well in Zhang et al.'s work [31]. The end result is a microstructure which imparts superior mechanical performance to the alloy.

This work aims to demonstrate the opportunity for the use of a new experimental method to capture multiple levels of microstructure evolution in Ti-6Al-4V alloy through miniaturised multi-directional open-die forging tests, meanwhile reaching higher temperature capability. The microstructure evolution is readily detailed through using complementary characterisation techniques, while FE modelling used to verify the stress and strain states within the specimens, as well as determine required compressive loads for the micro-cogging (*i.e.,* open-die forging) operations. Such a systematic combined approach could be employed for the development of future digital twins of open die forging of advanced engineering alloys and help inform process optimisation decisions in industry.

** Aerospace Technology Institute (ATI) creates the technology

strategy for the UK aerospace sector and funds world-class research and development.

2. Materials and methods

2.1. Material and open-die forging methods

The commercial α + β alloy Ti-6Al-4V was selected as the specimen material for the high temperature forging trials. The nominal chemical composition of the material is provided in Table 1. As an α + β alloy, Ti-6Al-4V can have differing volume fractions of α and β phases, depending on heat treatment and the contents of interstitial elements (primarily oxygen). The procured Ti-6Al-4V average Vickers microhardness was measured as 364HV across the longitudinal section and 376HV across the transverse section.

The alloy was procured as a 12 mm hot-rolled round bar. Anti-oxidising glass coatings were applied to sections of the alloy bar before being subjected to a heat treatment in a VFE TAV TPHF horizontal vacuum furnace for 2 h at 1100 °C followed by air-cooling. This heat treatment above the β-transus (about 1000 °C) was to grow the β grains drastically, to replicate the β recrystallised condition, which is typically the microstructure processed at industrial-scale by open-die forging. Henceforth, this material will be referred to as "as-heat-treated" (AHT). The AHT sections of bar were then machine cut into shorter test specimens with 28–35 mm length. The effect of heat treatment from the procured material to the AHT state is presented in Fig. 1, where the initial fully equiaxed microstructure of approximately 85% globularised α + 15% transformed β (*i.e.,* secondary-α) transitioned through a β recrystallised microstructure to an α lamellar structure with an average prior-β grain size of 700 μm. The billet (BD) and the cogging (CD) directions are denoted to highlight the directions at which the open-die forging was conducted.

The open-die forging was carried out on a 250 kN Zwick/Roell™ Amsler Z250 load frame equipped with a Severn Thermal Solutions SF2113 Split Furnace (SF) using a CU2113 Eurotherm™ temperature control system, and the Zwick™ testXpert III software. The manipulation of the specimens was carried out using an in-house developed miniaturised open-die forging manipulator, integrated into the tensile test machine, details of which are explained elsewhere [27]. Specimens were first mounted into the manipulator coupling and then aligned through the extensometer slot of the SF. Specimen positioning was then adjusted remotely prior to heating and the remaining gaps in the SF extensometer slot were filled with ceramic wool for thermal insulation. This set-up can be seen in Fig. 2.

The specimens were then heated to 950 °C within the SF and "soaked" thermally for 10 min to ensure a homogeneous and stable temperature distribution. A pre-load of 20 N was applied at the end of the soak time, to aid against specimen slipping. The specimens were then repeatedly deformed in 5% cross-section height reduction increments (*i.e.,* in the CD) using a controlled step program. To simulate the cogging (*i.e.,* open-die forging) operation, the specimen was rotated 90° (except where specified otherwise) between each compression (or "bite"). 0° indicator markings were added to the manipulator rods in vision of the operator so that specimen rotation could be tracked between bites, an example of this is presented in Fig. 2(b). The test matrix for all the cogging operations conducted on the Ti-6Al-4V specimens is provided in Table 2.

The final cogged geometry target for the most deformed specimen, SP7, was for a reduction of 25% in nominal cross-section in CD, corresponding to a macroscopic true strain(ε_m) of 0.22, with a measured crosshead displacement rate of 0.12 mms^{-1}. The specimen was then withdrawn from the split furnace and allowed to air cool. A schematic diagram of the thermomechanical procedure for the forging tests is shown in Fig. 3(a).

Following forging, the 3D geometries of the specimens were captured using the GOM ATOS TripleScan III non-contact rotary table scanner. GOM Suite software was used to measure the cross-section reduction for each sample using section areas taken every 1 mm along the sample. The average cross-section reduction was then calculated from the difference in area between sections in the stub zone against the cogged zone.

A pair of custom-manufactured platens were used as compression dies at elevated temperature. The cylindrical platens, 20 mm in diameter 15 mm in height, were manufactured by wire electric discharge machining (EDM) from Nimonic®-90 nickel-based superalloy. The internal volume of the vertical split-tube furnace determined the maximum platen size used in these experiments. The inner diameter of the furnace was 80 mm, and the platen size had to allow for adequate space for the specimen coupling at the end of the manipulator rod, allowing the placement of specimens over the entire span of the die surface to protect tooling from uneven loading.

Two manipulator rods, 6 mm in diameter, were manufactured for high temperature testing. Cylindrical couplings were used to transmit the rotational motion from the stepper motor to the manipulator rods and, hence, test specimens. The manipulator rods were manufactured from Nimonic®-90 superalloy exclusively for these tests.

Cylindrical coupling sets were created and attached on opposite ends of the manipulator rods for holding of the specimens during the cogging operations. These 8 mm–12 mm bore diameter cylinders were machined from Nimonic®-90 superalloy using wire EDM. All couplings were designed and manufactured with threaded grub screw holes for the manipulator rod and test specimen assembly. All grub screws for high temperature experimentation were also manufactured from Nimonic®-90 superalloy.

The high temperature testing in this study was completed at 950 and 1050 °C. To extend the longevity of the Nimonic®-90 superalloy platens, boron nitride suspension was used as a lubricant and anti-stick agent. Images showing the tooling dies, rods, and couplings after testing are shown in Fig. 2(f)–(h), demonstrating the effect of repeated compressions on the lubricant across the dies and specimens. Additionally, thermal images captured during and after testing of the tooling are presented in Fig. 2(d)–(e), showing minimal conduction along the length of the manipulator rod. This demonstrates that there is sufficient distance between the SF and electrical components of the cogging apparatus.

2.2. Finite element analysis

A 3D finite element method (FEM) model of the cogging tests, including the preliminary heating and soaking stages, was performed using DEFORM™ software to predict the stress and strain distributions along the samples at different locations, as well as generate the load *vs.* time plots. Material data for the respective forging strain rates and temperatures was captured in the lab through standard compression testing. The flow stress was calculated for validation using the 0.2% proof stress method and was found to align closely with the flow stress data available within DEFORM™ and published works [32].

A thermal conductivity range of 6.9–18.0 $Wm^{-1}K$ for Ti-6Al-4V was used as a function of temperature for heating operations of the workpiece as suggested by DEFORM™ which are values corroborated in the work of Kim & Lee [33], with a convection coefficient of 0.02 $Ns^{-1}mm^{-1}{}^{\circ}C^{-1}$. A friction coefficient of 0.3 between the dies and the workpiece was utilised based on values for lubricated hot forging suggested by DEFORM. The simulations were set up with isothermal conditions with no heat transfer between the workpiece, die, and environment. A Taylor-Quinney factor of 0.9 was used [34,35], which is a good estimate of the fraction of heat converted from mechanical work

Table 1
Nominal chemical composition of the Ti-6Al-4V alloy.

Element	Ti	Al	V	C	Fe	O	N	H
Weight %	Bal.	5.80	4.00	0.08	0.30	0.20	0.05	0.01

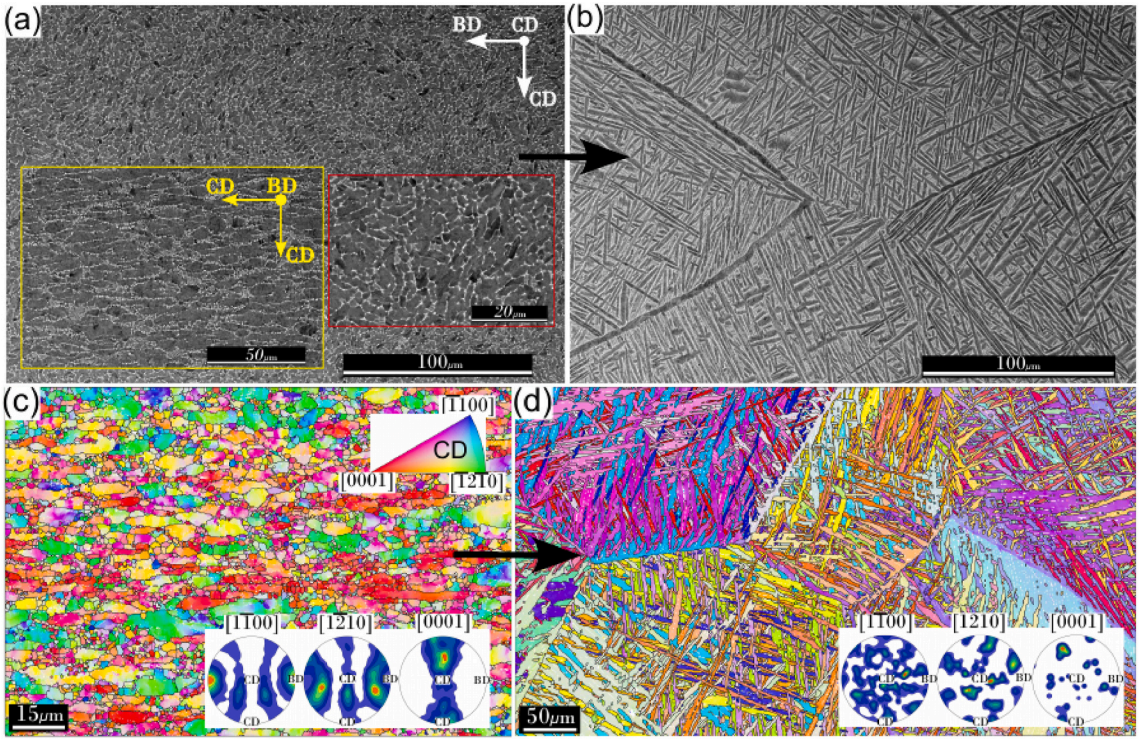

Fig. 1. (a) Backscatter electron images of procured Ti-6Al-4V material prior to heat treatment showing a fine microstructure, a higher magnification image highlighted in red, and an image showing the transverse microstructure highlighted in yellow (b) Backscatter image of AHT microstructure, showing α colonies within prior β grain boundaries, (c) EBSD IPF-CD map (out-of-page) of procured Ti-6Al-4V material prior to heat treatment, highlighting a fine hot-rolled microstructure with clear texture observed in pole figures, (d) EBSD IPF-CD map (out-of-page) of AHT Ti-6Al-4V material, highlighting a microstructure of α lath colonies within prior β grain boundaries with no discernible texture observed in the pole figures. Orientation directions are the same unless highlighted in blue, IPF-CD (out-of-page) key is the same for (c) and (d).

during deformation [36–38]. A mesh with 120,000 tetrahedral elements was created for the geometry of the workpiece. Throughout the experimental compression tests, the movement speed of the lower die was recorded before being entered into the FEM simulation.

The model for this study was first set up for nominal cogging conditions, assuming all rotations and compressions were perfect 5% incremental bites throughout with no slippage or sticking, shown in Fig. 4 (a). A second model was set up post experimentation for Specimen SP7, which had a sticking complication during testing. This sticking was due to numerous factors, including the large number of bites, which resulted in the final rotation being interrupted. The final compression was repeated in the first compression direction. Therefore, this element was carried forward into the model and the simulation repeated, these results can be seen in Fig. 5.

The specimens' dimensions predicted from the simulation were compared by the real dimensions of the deformed specimens after testing. The simulation was set up to replicate the same compression measurements of the specimen range up to a macroscopic true strain(ε_m) of 0.26. The results of FE simulation match the geometry of the cogged specimens, and for Specimen SP7 the simulations predicted a final cross-section of 8.5 mm in one direction, which was within 2% of the measured diameter of 8.3 mm. This suggests that the strain distribution is reasonably accurate and validates the chosen heat transfer coefficient and friction coefficient values, as well as the chosen plasticity model.

2.3. Microstructure characterisation methods

The deformed specimens were cut along the longitudinal axis using EDM. They were then cold-mounted in non-conductive epoxy resin and ground using silicon carbide abrasive papers. This was followed by polishing with 0.02 μm colloidal silica suspension to a mirror finish. The specimens were subjected to a final etching by Kroll's reagent (*i.e.,* 100 mL water, 1–3 mL hydrofluoric acid, and 2–6 mL nitric acid). A Leica™ DM12000 microscope with a motorised stage was then used to acquire light micrographs of the specimens. A macro image of the entire sample was captured, and then higher magnification micrographs were captured in three zones: stub, transition, and cogged regions. The mean linear intercept method [39,40] was used within ImageJ software to measure the average grain size in the stub and cogged zones.

Following this, the specimens were also hot-mounted in conductive Bakelite, then ground and polished to a mirror finish, before being subjected to a vibratory polish for 16h using 0.02 μm colloidal silica suspension diluted to 20% with deionised water. A Thermo Fisher Scientific™ Quanta 250 field emission gun scanning electron microscope (FEG-SEM), with an Oxford Instruments™ Nordlys EBSD detector, and the Oxford Instruments™ AztecHKL 4.1 software was used to acquire EBSD data maps. This allowed qualitative evaluation of the microstructural changes in the Ti-6Al-4V alloy.

The globularised fraction in each sample was measured using a manual point counting method (i.e., following ASTM E562). A rectangular grid of 100 points was superimposed onto the electron backscattered images obtained at 800x magnification. The thickness and length of the grains intersecting the grid points were measured using ImageJ software. The aspect ratio of each grain was then calculated, and a ratio of 2 was taken as a limit to consider grains as globularised.

A range of map areas was captured for every sample at locations within the cogged zone. In all cases, at least 80% of the points were successfully indexed. The captured EBSD data was analysed using the MTEX Toolbox [41] developed in the MATLAB® software package. High angle grain boundaries (HAGBs) were identified based on misorientation angles of >10°. The low angle grain boundaries (LAGBs) were classified if the misorientations lay in the range between 3° and 5°, whereas medium angle grain boundaries (MAGBs) had misorientation angles between 5° and 10°.

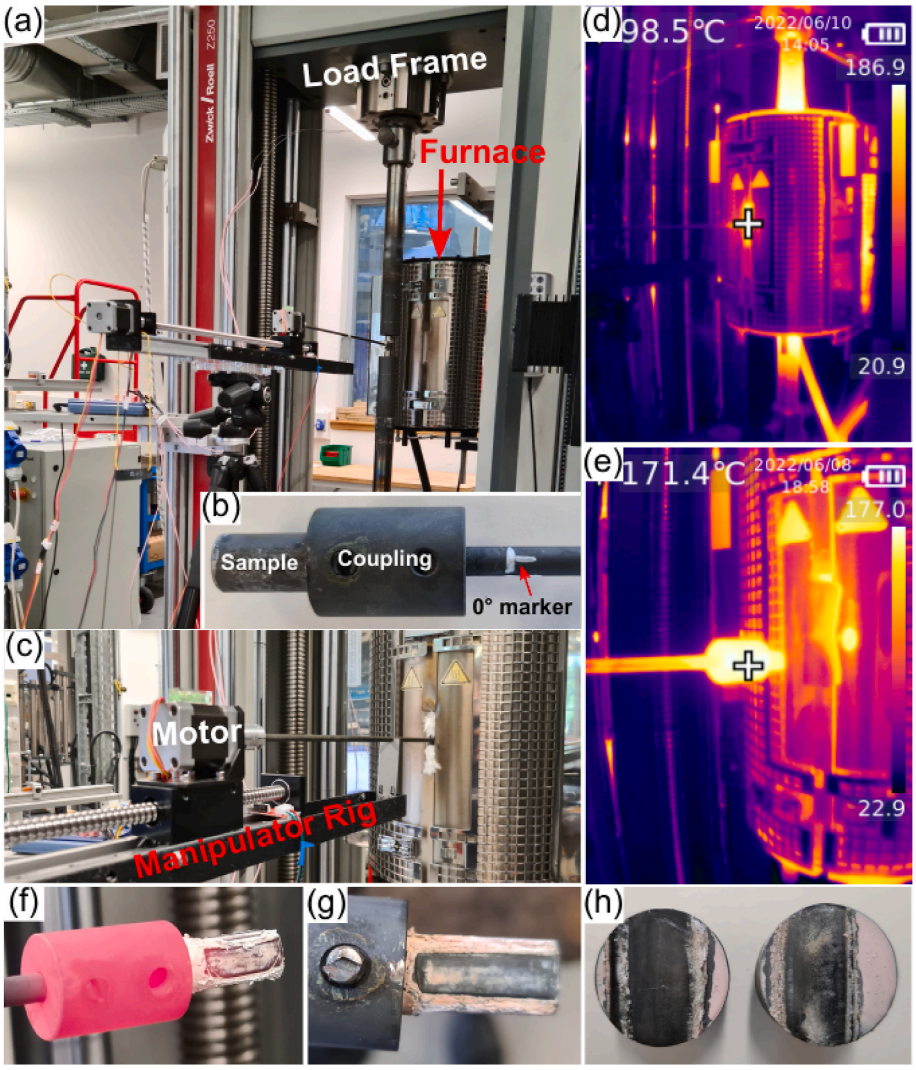

Fig. 2. Details of the experimental setup for the reduced-scale cogging trials: (a) the test apparatus during alignment within Zwick/Roell™ Z250 load frame prior to testing, (b) a close-up of sample in coupling, highlighting a 0° rotation marker, (c) close-up of the apparatus manipulator during high temperature testing. Thermal camera image of split-tube furnace taken; (d) during testing highlighting heat escaping through insulated extensometer slot and, (e) after testing and during cooling, highlighting the effective heat dissipation from the sample and coupling along the manipulator rod. Captured using the Uni-T UTi690B Professional Thermal Imager (−20–550 °C). Images showing test specimen mounted within the manipulator coupling, highlighting removal of lubricant during specimen deformation; (f) immediately after removal from furnace after forging and, (g) after air cooling, (h) Nimonic®-90 superalloy custom dies after testing.

Table 2
Test matrix for Ti-6Al-4V alloy, deformed at hot temperatures, detailing the number of bites, targets for cross-sectional height reduction, and specimen geometries.

Specimen No.	SP1	SP2	SP3	SP4	SP5	SP6	SP7	SP8	SP9	SP10	SP11
Target Reduction in Cross-CD (%)	5	10	10	10	15	20	25	5	10	10	15–30
Target Geometry	Square	Square	Square	Square	Square	Square	Square	Oct	Oct	Square	Square
Total No. of Bites	2	4	4	6	6	8	10	4	8	4	12
Temperature (°C)	950	950	950	950	950	950	950	950	950	950	950 & 1050

A DuraScan® 70 G5 hardness tester was used to capture micro-hardness maps. For this, a load of 1 kg (HV1) was used over a dwell time of 10s in accordance with the Vickers BS EN ISO 6507 [42] standard for all specimens. The obtained hardness maps were superimposed over the light micrographs to facilitate comparison of the grain structure against hardness. Indentations were made every 1.7 mm for maps and 0.7 mm for line series measurements.

3. Results

3.1. Miniaturised open-die forging results

Table 3 presents the geometric results from the open-die forging of the mini-billets, highlighting the differences in cross-section reduction targets against the measured cross-section reductions in the lab and using 3D GOM scan data. The deformation of all cogging trials followed a similar overall trend. This can be seen from the load graph data presented in Fig. 6(a). The post-analysis load graph simulated using DEFORM™ for the material under idealised conditions is provided in

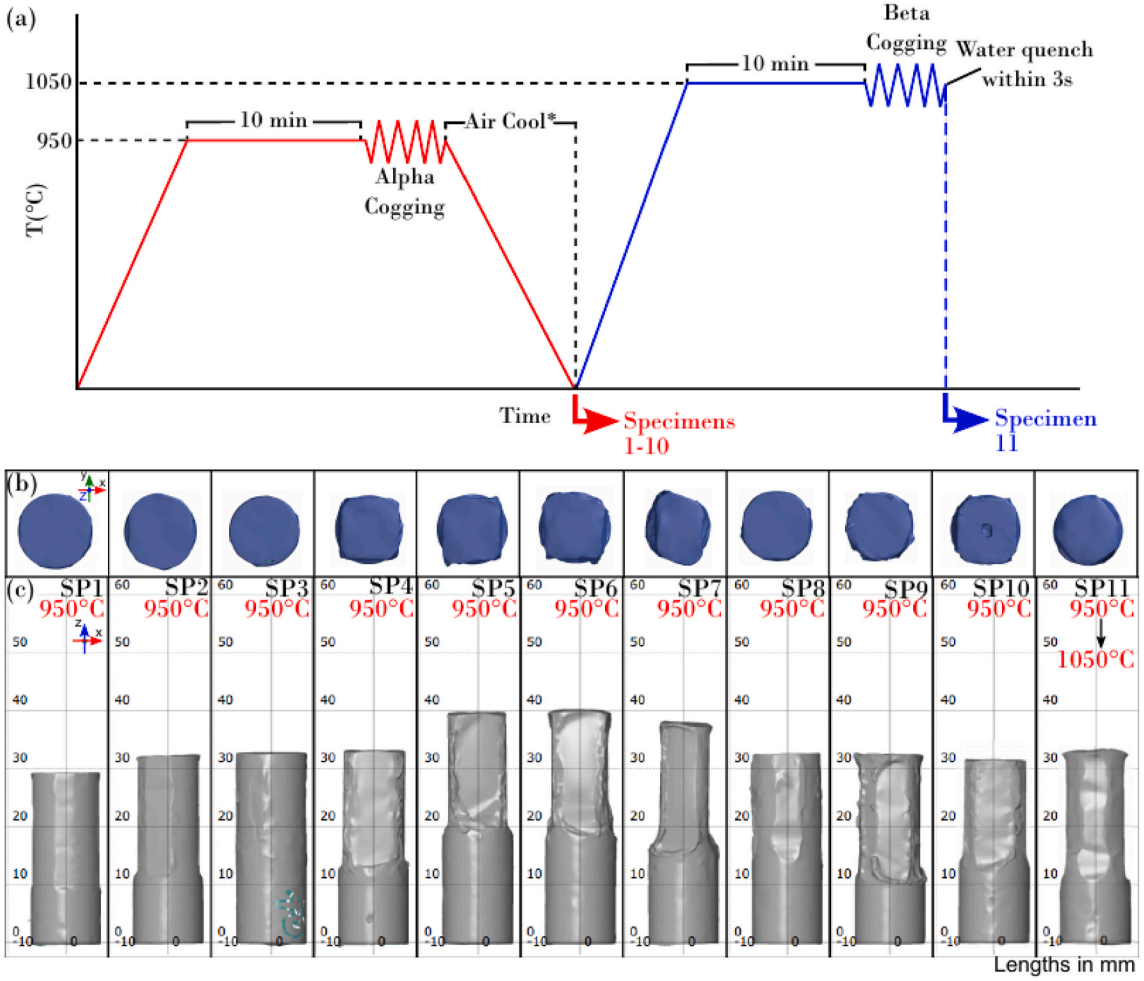

Fig. 3. a) Schematic representation of the sub-transus (950 °C) processing and the super-transus (1050 °C) processing used in this study. 3D GOM photogrammetry scans of the specimen range highlighting the final forged geometries, showing (b) plan (blue) and, (c) elevation views (grey). All specimens are presented to the same scale.

Fig. 6(l). The predicted test time for the FE load graph in Fig. 6(b) is much shorter, and the load increases more uniformly for each set of bites. N.B. Specimen SP3 was off-centre during alignment (due to new methods being tested for in-situ alignment) which led to it slipping relative to the dies during compression, this is reflected in Fig. 6(c). A final observation is the large decrease in required load seen in Fig. 6(j) due to the temperature increase from 950 to 1050 °C for cogging above the β-transus, the period of cooling and reheating has been removed from this load graph.

3.2. Microstructure characterisation results

GOM 3D scan results for each of the Ti-6Al-4V specimens are compared in Fig. 3(b)–(c). It can be seen that the final billet geometries are representative of billet geometries seen in industrial processes [43]. N.B. A thin layer of boron nitride lubricant can be seen on the 3D GOM scans across the samples, which has caused observed ridges.

A noticeable increase in the Vickers hardness was observed for all samples at the edges that have been exposed to air during forging, *e.g.,* an average increase of 10–20% across all samples. This increase in Vickers hardness is due to the formation of oxygen-rich alpha-case layer at the surface of the specimens cogged at high temperature. It is evident from the captured Vickers hardness maps and lines that overall, there is no clear change from the forging itself. This could be indicative of an increase in strength with no measurable change in ductility within the more highly strained specimens, as the grain size decreases while the hardness values remain the same.

The FE simulation results shown in Figs. 4 and 5 highlight the strain distributions expected over the specimen's range. The 30% target was selected as this is just beyond the upper limit of the current Ti-6Al-4V dataset and is typically the upper limit of cross-section reduction seen in industrial cogged billets.

Fig. 7 presents electron-backscatter micrographs from the three separate zones within specimen SP7 where changes in morphology are observed. These observations are shown at three separate magnifications, where the original lamellar/α-platelet structure of the AHT material in the stub zone is seen to break down and form rounded globularised α grains. Internal localised strain is observed within the larger α lamellae seen at the transition zone edges of the specimen, indicating lamella breakdown *i.e.,* the first stage of globularisation.

Fig. 8 presents results from specimen SP10, which was used as an exploratory sample to investigate the level of adiabatic heating released in the centre of the sample during compression. This was achieved by machining a small hole in the end of the sample to place a thermocouple into the end of the specimen that was to be forged. Fig. 8(c) shows a light micrograph of the specimen with the thermocouple hole visible in the cogged zone, with an overlaid Vickers microhardness map. A noticeable increase in hardness is observed at the edge of the specimen, where the α-case has formed through diffusion with the hot air of the furnace. The band contrast map seen in Fig. 8(a) is also presented. The band contrast reveals another example of the large volume of α-case generated at the edges of the sample exposed to air during forging, as well as the

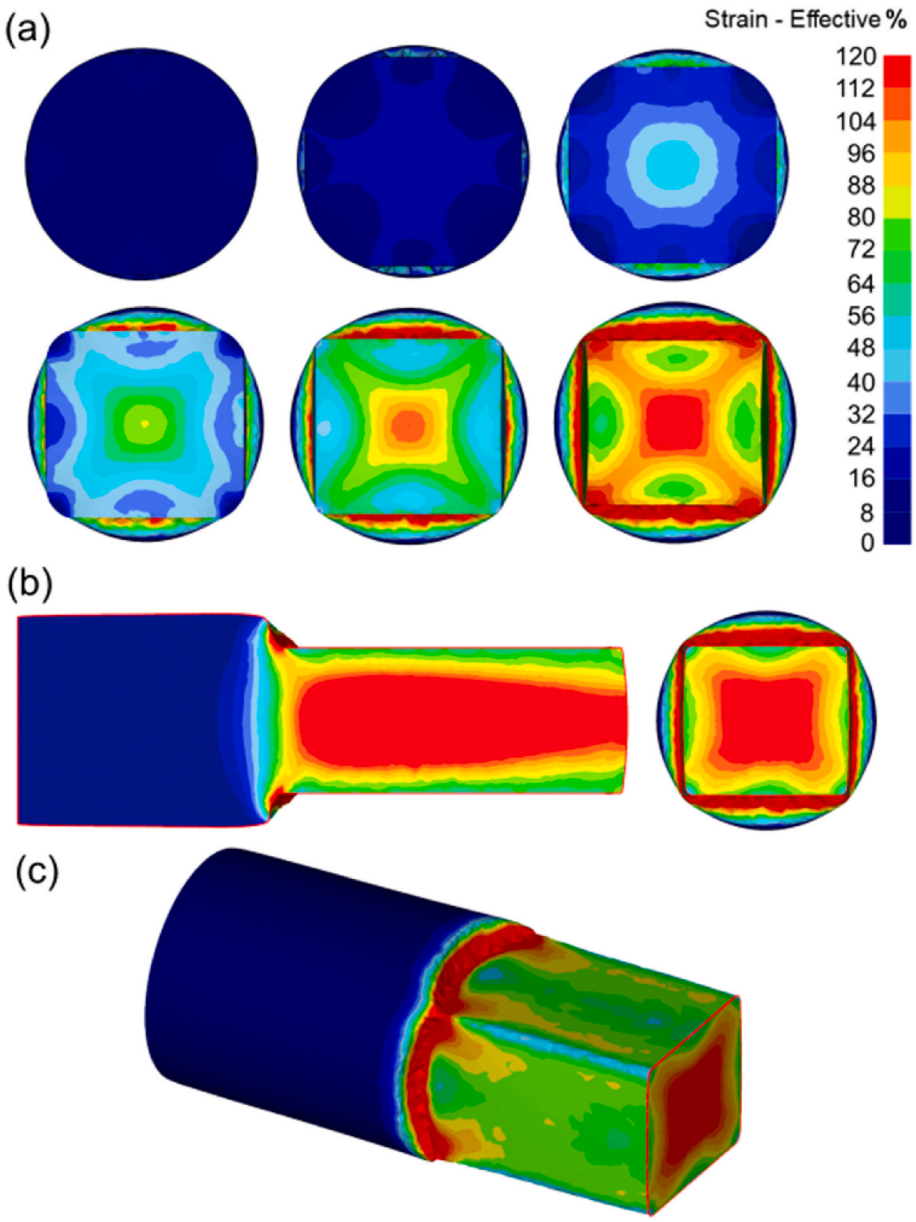

Fig. 4. The results of FE simulation presenting (a) the nominal strain distributions on the radial cross-section after each 5% cogging pass up to 6 passes (*i.e.,* 30% cross-section reduction), (b) the strain distributions on both the longitudinal and transverse cross sections of Ti-6Al-4V specimen following cogging testing to 30% cross-section reduction and, (c) effective strain distribution in 3D isometric view. The effective strain scale bar is the same for all plots.

numerous fine α-lamellae that formed from the initial β recrystallisation heat treatment. Lastly, Fig. 8(b) shows the plot of temperature (°C) against time (ms) which highlights the small increase in temperature (~3 °C) which is about double the increase measured by the set of thermocouples elsewhere in the furnace.

The initial lamellar structure of the AHT material that was created during the β recrystallisation heat treatment has been retained in the cogged zone of specimen SP1, shown in Fig. 9(a). The local strain induced in the billet is too low to have had significant impact on the microstructure. Fig. 9(b)–(d) reveals two stages of globularisation in each micrograph, where both long platelets with grooving and fully globularised equiaxed grains are observed, suggesting that the operating globularisation mechanisms are orientation dependent. It is also indicative that at low strain level, a high degree of globularisation can be achieved through the activation of different slip systems by the multi-directional compression. Fig. 9(e) and (f) demonstrate some fully globularised/equiaxed grains as the strain level has reached a sufficient level so that a large fraction of the grains have been broken down and globularised. The observed globularisation mechanisms comprise shearing of α laths and boundary splitting. The strain path has been reported to have various effects on the kinetics of globularisation. In the present study we observed similar kinetics as those during uniaxial testing reported by Shell and Semiatin [44].

A final exploratory test was the forging of specimen SP11. This specimen was the first advancement into forging above 1000 °C using the miniaturised cogging setup. Testing the temperature limitations of the tooling was one key output from this test. However, it also allowed the investigation into the β cogging of the Ti-6Al-4V alloy at this scale.

Fig. 10 presents three magnification levels of EBSD IPF-CD (out-of-page) map data that show a Widmanstätten (or basketweave) structure, in Fig. 10(d) this structure is observed along the centre of the specimen in the BD, understandably where some diffusion was allowed to occur due to the higher temperature retention of the core, and thus slower cooling rate. On the other hand, the outer regions of the specimen are

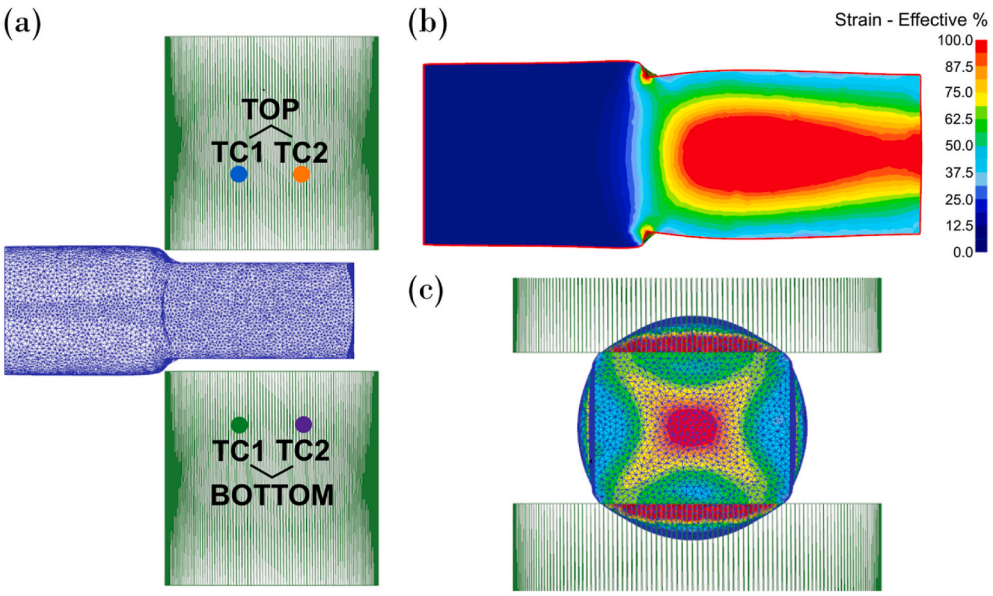

Fig. 5. Results of FE simulation of Specimen SP7; (a) an illustration of the FE mesh for the workpiece and dies at 25% reduction with repeated final compression in the CD at 0° rotation, also highlighting representative thermocouple placements for reference in Fig. 8, (b) strain distributions on the longitudinal cross-section following cogging to 25% reduction with repeated final compression in the CD at 0° rotation, (c) strain distributions on the transverse end, including mesh on the specimen and dies.

Table 3
Geometric assessments for all Ti-6Al-4V specimens cogged at elevated temperatures, comparing the target cross-sectional height reduction, lab measured cross-sectional height reduction measured with Vernier calipers, and the maximum and average cross-sectional area reductions calculated using sectioned areas from the stub and cogged zones of the 3D GOM scans. Also detailing the geometry, total number of bites, and calculated elongation percentage.

Specimen No.	SP1	SP2	SP3	SP4	SP5	SP6	SP7	SP8	SP9	SP10	SP11
Target Reduction (%)	5	10	10	10	15	20	25	5	10	10	15/30
Measured Reduction (%)	3.8	6.2	0.6	10.8	12.9	14.5	13.4	2.4	8.9	9.0	18.3
Avg. Area Reduction (%)	1.3	2.3	0.2	4.2	8.1	10.8	12.2	0.1	7.3	3.6	13.1
Max. Area Reduction (%)	1.4	3.9	0.3	4.8	8.1	11.0	15.4	0.4	7.4	3.9	15.1
Geometry	Square	Square	Square	Square	Square	Square	Square	Oct.	Oct.	Square	Square
Total No. of Bites	2	4	4	6	6	8	10	4	8	4	12
Elongation (%)	0.7	1.3	0.5	4.1	2.2	5.0	7.1	0.6	5.9	4.0	10.3
Temperature (°C)	950	950	950	950	950	950	950	950	950	950	950 & 1050

observed to be martensitic, where the water-quenching did not allow time for diffusion, which aligns with Bignon et al.'s study on martensite formation in titanium alloys [45]. This was due to the rapid cooling from above the β-transus after forging, which inhibited the growth and recrystallisation of secondary α grains. It is also clear within the presented pole figures that no discernible texture can still be observed after deformation. The prior β grain structure is also visible within Fig. 10(c), where the α-colonies would nucleate from the grain boundaries.

For all samples examined in this work, the extent of microstructural transformation becomes more pronounced with increasing levels of deformation and local effective strain. After two orthogonal deformation steps of 5%, *i.e.,* in specimen SP1, the initial microstructure of the AHT material that was created during the β-recrystallisation heat treatment remains largely unaffected, as shown in Fig. 9(a). At higher levels of deformation, for example in specimens SP4, SP5, and SP6, where the effective strain in the cogged zone reaches between 0.25 and 0.9, some deformed α laths and segmentation are observed, as shown in Fig. 9(b)–(d); but these occurrences remain isolated. Sample SP7 underwent the highest amount of deformation, *i.e.,* effective strain of 1.37 in the cogged zone, and displayed the most deformed microstructure. Many alpha laths are broken up into smaller equiaxed grains, observed in Fig. 9(e); and as a result, the globularised α fraction rose to 28%. However, full globularisation was not achieved in this sample and some initial alpha lamellae remained.

PBGR, provided in Fig. 11, was carried out using the MTEX Toolbox which recovers the parent grains from the measured child grains using the Burgers orientation relationship [46]. This aligns the (110) plane of the β phase (*i.e.,* BCC crystal structure) with the (0001) plane of the α-phase (*i.e.,* HCP crystal structure) and the $[1\bar{1}1]$ direction of the β phase with the [2110] direction of the α phase. It can be observed that the success of the software in recovering the parent grains is influenced by both the temperature and localised strain in the material. Fig. 11(a)–(b) display that a clear reconstruction is obtained if there is no plastic strain, or if there is deformation above the β-transus, whereas in Fig. 11 (c)–(e), the reconstruction becomes increasingly interrupted with α-platelets whose orientations differ significantly from their neighbours within the same α-colonies. These interruptions become more frequent as the cross-section reduction, and hence level of strain, increases. This trend continued with specimen SP7, although the prior-β grains could be discerned visually from EBSD IPF maps, the computation of the PBGR was less effective at discerning some parent grains, with a greater failure rate observed, *i.e.,* more white pixels in Fig. 11(f).

Fig. 12 shows a comparison of the different shape parameters seen between low strain specimen SP2 (2.3% cross-section reduction) and the most highly deformed (12.2% cross-section reduction) specimen SP7 EBSD data. It can be clearly seen that the difference in α grain shape, also displayed in Fig. 12(g)–(h) is the grain size distributions between the low strain and high strain material. The equivalent perimeter is defined as the perimeter of a circle with the same area as the grain and is always

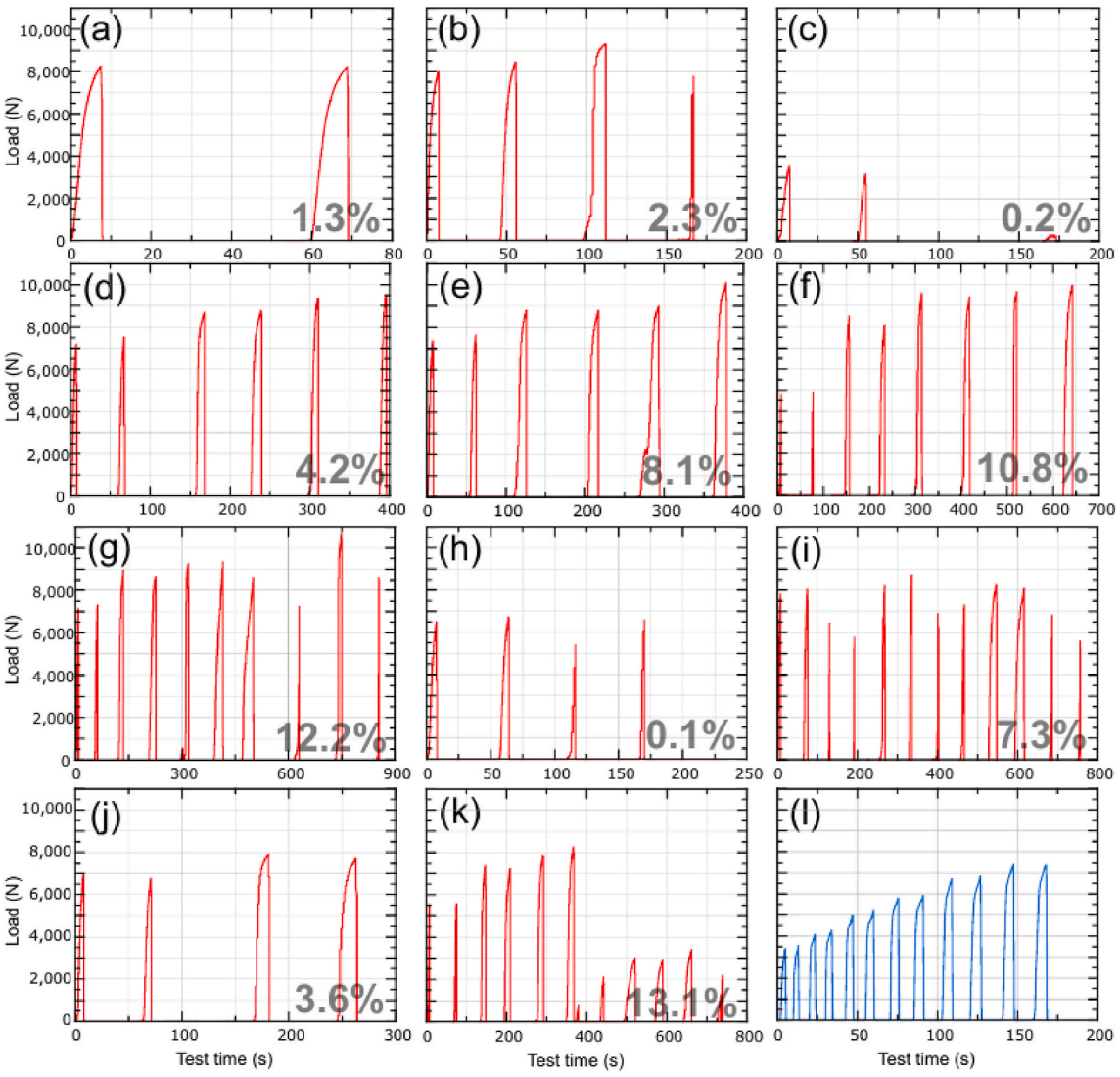

Fig. 6. Measured load (N) against test time (s) during cogging tests for specimens; (a) SP1 (5%), (b) SP2 (10%), (c) SP3 (10%), (d) SP4 (10%), (e) SP5 (15%), (f) SP6 (20%), (g) SP7 (25%), (h) SP8 (5%), (i) SP9 (10%), (j) SP10 (10%), (k) SP11 (15/30%). Data was taken from Zwick/Roell™ load cell during testing, recorded in Zwick™ testXpert III software. The values on the plots are the measured deformation (%), compared to the target deformation (%) stated in brackets in the caption for each specimen, (l) The FE predicted graph for load (N) against number of steps for Ti-6Al-4V alloy to the same number of bites. All plots are to the same y-axis scale and visualised using LabPlot by KDE®.

smaller than the actual perimeter of the grain. Therefore, the ratio between grain perimeter and equivalent perimeter, known as the shape factor, is always greater than one. Fig. 12(c)–(d) shows the shape factor, *i.e.,* how different each grain is from a circle.

Similarly, Fig. 12 (e)–(f) displays the discrepancy between the actual grain shape again a circle using the perimeter (P) and equivalent perimeter (P_e) in a simple calculation:

$$\frac{P - P_e}{P} \tag{5}$$

this plots symmetric grains as values close to zero and oblong or irregular convex grains will get values up to 0.5.

Investigations on the modelling of α globularisation in titanium alloys have received significant attention; however, few models available in the literature are practical for use in industrial applications. Some robust physical models based on mechanisms like boundary splitting or termination migration yield appropriate predictions [47,48]. However, these models require knowledge of the length and thickness of α laths and produce a time for the completion of the microstructural mechanisms rather than a globularised fraction, so they are not the most practical. Avrami's equation is often present in the modelling of recrystallisation and globularisation [49–52] but it is often based on uniaxial testing trials and not transferable to the industrial cogging process that includes changes in strain path. Dislocation density models are also used for microstructural modelling [53–55] with reasonable accuracy during uniaxial testing.

An in-house model was developed based on the dislocation density model from Sun et al. [56], compiled in the formats presented in equations (1)–(4). The dislocation rate takes into consideration work hardening, dynamic recovery, static recovery, and dynamic globularisation, and these mechanisms are represented by the four terms in equation (2). The globularisation rate is dependent on the dislocation density, temperature, grain size, and a parameter γ that varies with dislocation density and level of globularisation. Globularisation occurs only when the dislocation density is higher than a critical value depending on these process parameters.

The parameters of this globularisation model were determined from experimental data [57] using a genetic algorithm optimisation approach in Microsoft Excel and are presented in Table 4. The experimental data used for calibration is from multiaxial forging trials on large samples, so

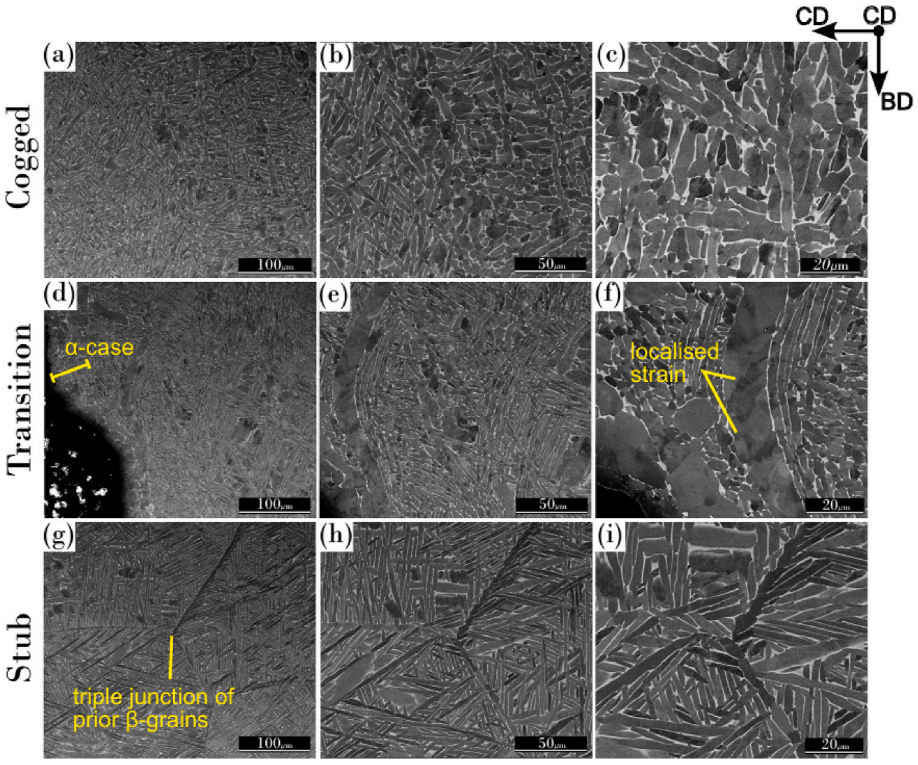

Fig. 7. Backscatter electron images taken from different zones of the cross-section of specimen SP7 after forging at three magnification levels: (a)–(c) Cogged zone, (d)–(f) Transition zone, (g)–(i) Stub zone. Highlighting effect of cogging, using the manipulation apparatus, on the microstructure obtained at different strain zones within a single specimen.

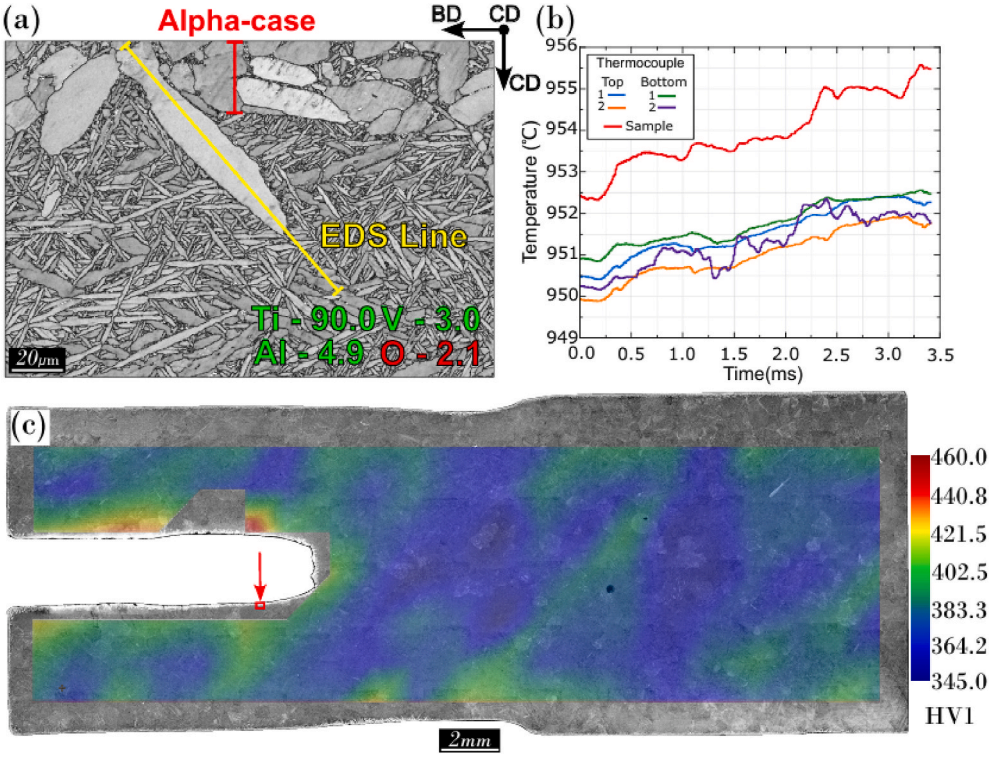

Fig. 8. (a) A band contrast micrograph of Specimen SP10 from internal face edge of the thermocouple hole showing large α lamellae, (b) Temperature(°C) against time(ms) from thermocouples in the sample and top and bottom dies during compression (representative thermocouple placements shown in Fig. 5) and, (c) light micrograph of Specimen SP10 showing the location from which (a) was captured and overlaid Vickers microhardness map.

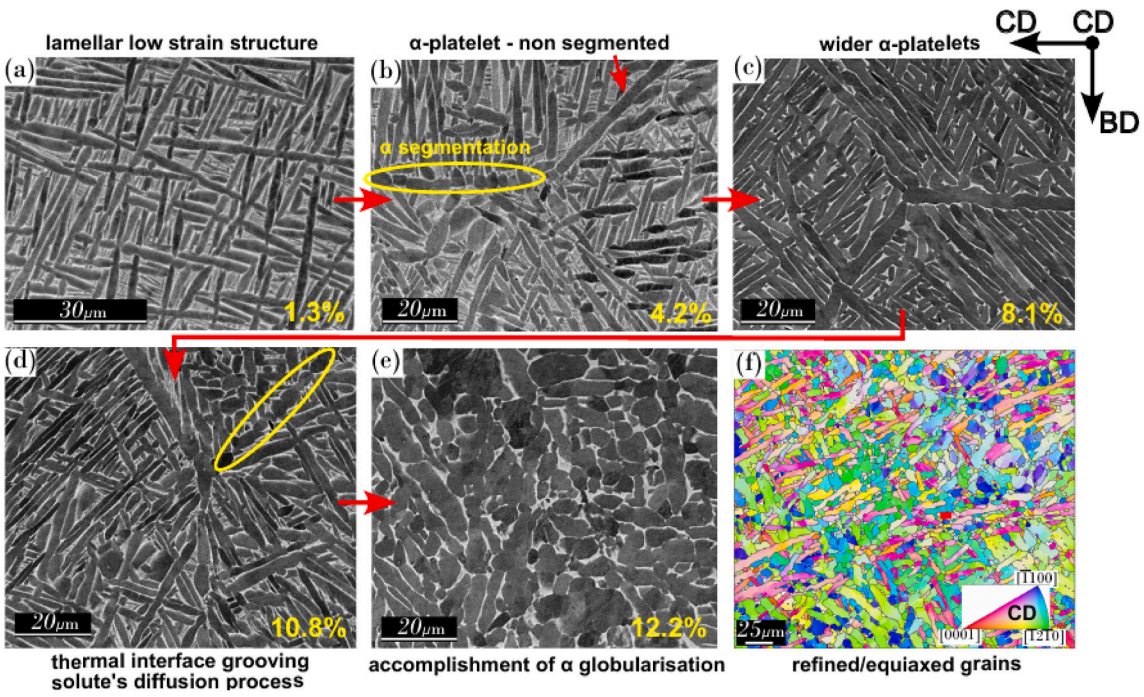

Fig. 9. Microstructure appearances of the Ti-6Al-4V specimens underwent different levels of globularisation with increased average cross-section reduction (*i.e.,* strain), denoted in caption brackets, (a) SP1 (1.3%), (b) SP4 (4.2%), (c) SP5 (8.1%), (d) SP6 (10.8%), (e) SP7 (12.2%), and (f) EBSD IPF-CD (out-of-page) map showing segmented α and equiaxed grain orientations of Specimen SP7 (12.2%).

the prediction should be more accurate for trials similar to an industrial cogging process scale.

It was then implemented as a user subroutine into Finite Element software DEFORM™ and executed alongside the process modelling simulations. Predictions from this model for the experimental conditions in this work are presented in Fig. 13. The predicted values are on trend with the experimental levels of globularisation. N.B. The first two experimental data points are >0% globularisation due to the measurement method, where α-laths orientated in the out-of-page image plane result in a grain aspect ratio of <2, meaning the true % globularisation is closer in correlation with the model results for <0.3 effective strain.

$$\rho = \dot{k}_1\sqrt{\rho}\dot{\varepsilon} - k_2\rho\dot{\varepsilon}^m \exp\left(\frac{-Q_s}{RT}\right) - k_3\rho^n \exp\left(\frac{-Q_s}{RT}\right) - \frac{k_4\rho\dot{S}}{(1-S)} \quad (1)$$

$$\dot{S} = \frac{\beta_1\gamma\rho \exp(-Q_b/RT)}{d} \quad (2)$$

$$\rho_{cr} = \beta_2\left[\dot{\varepsilon}\exp\left(\frac{Q_z}{RT}\right)\right]^{\lambda_1} \quad (3)$$

$$\gamma = (0.1+S)^q(1-S)\frac{\rho}{\rho_{cr}} \quad (4)$$

Where ρ is the dislocation density (m^{-2}), Q_s, Q_b, Q_s are activation energies (J/mol/K), ρ_{cr} is the critical dislocation density (m^{-2}), S is the globularised fraction, γ is the mobile fraction of grain boundaries, R is the ideal gas constant (8.314 J/mol), k_1, k_2, k_3, k_4, n, m, p, q β_1, β_2, and λ_1 are constants.

4. Discussion

The presented pilot studies using the described new apparatus have successfully demonstrated the ability to characterise and control microstructural evolution during small scale open-die forging (*i.e.,* micro-cogging) of Ti-6Al-4V dual-phase alloy, as previously demonstrated with copper C101 [27] alloy (*i.e.,* at lower temperatures). Notably, the studies have proven and assessed the capability of this small-scale set-up to achieve a high degree of α-globularisation. This is exciting, as globularisation kinetics in Ti-6Al-4V remain of high research interest, as seen in the work of Ouyang et al. with the experimental and numerical simulation study of lamellar globularisation for titanium TC21 alloy [58], and also seen in the work of Jin et al. with additively manufactured Ti-6Al-4V [59]. With the increased throughput of testing that this apparatus can offer, this means research on this topic could be accelerated.

While it must be acknowledged that a 1:1 scale comparison with industrial ingot-to-billet conversion is impossible to replicate at this scale, *i.e.,* due to the industrial billet grains being centimetres in scale [60], the developed apparatus and methodology can still provide a useful tool for the simulation and testing of industrial scale processing parameters and the measuring of their impact on the existing material and structures. Specifically, the apparatus is capable of replicating the conditions and microstructural evolution during the later stages of ingot-to-billet conversion when some degree of microstructure refinement has already been achieved, *e.g.,* multi-directional forging of Ti-6Al-4V by Zhang et al.[22] Furthermore, the comparative simplicity and low-cost of the equipment, assuming existing access to suitable load frame/press and furnace, the methodology and tooling can be upscaled and modified to allow testing of larger specimens with coarser microstructures. Overall, the parameters that can be assessed with this equipment offer attractive benefits to industrial ingot-to-billet manufacturers as they can save largely on cost, material, labour, and time.

This method can also offer researchers an avenue for metallurgical processing studies. To date, especially in Ti-6Al-4V, ingot-to-billet conversion has been limited due to the large costs involved in producing specimens for characterisation and study. The high degree of control under isothermal conditions on offer with this method is significant, as it is distinctly relevant to the high thermal mass ingots found in industrial ingot-to-billet conversion. The low strain rate ($0.01s^{-1}$) used in this study is also representative of industrial ingot-to-billet conversion, as low strain rates are typical due to the large size of the ingots. Typically, higher strain rates are only observed in closed-die operations. However,

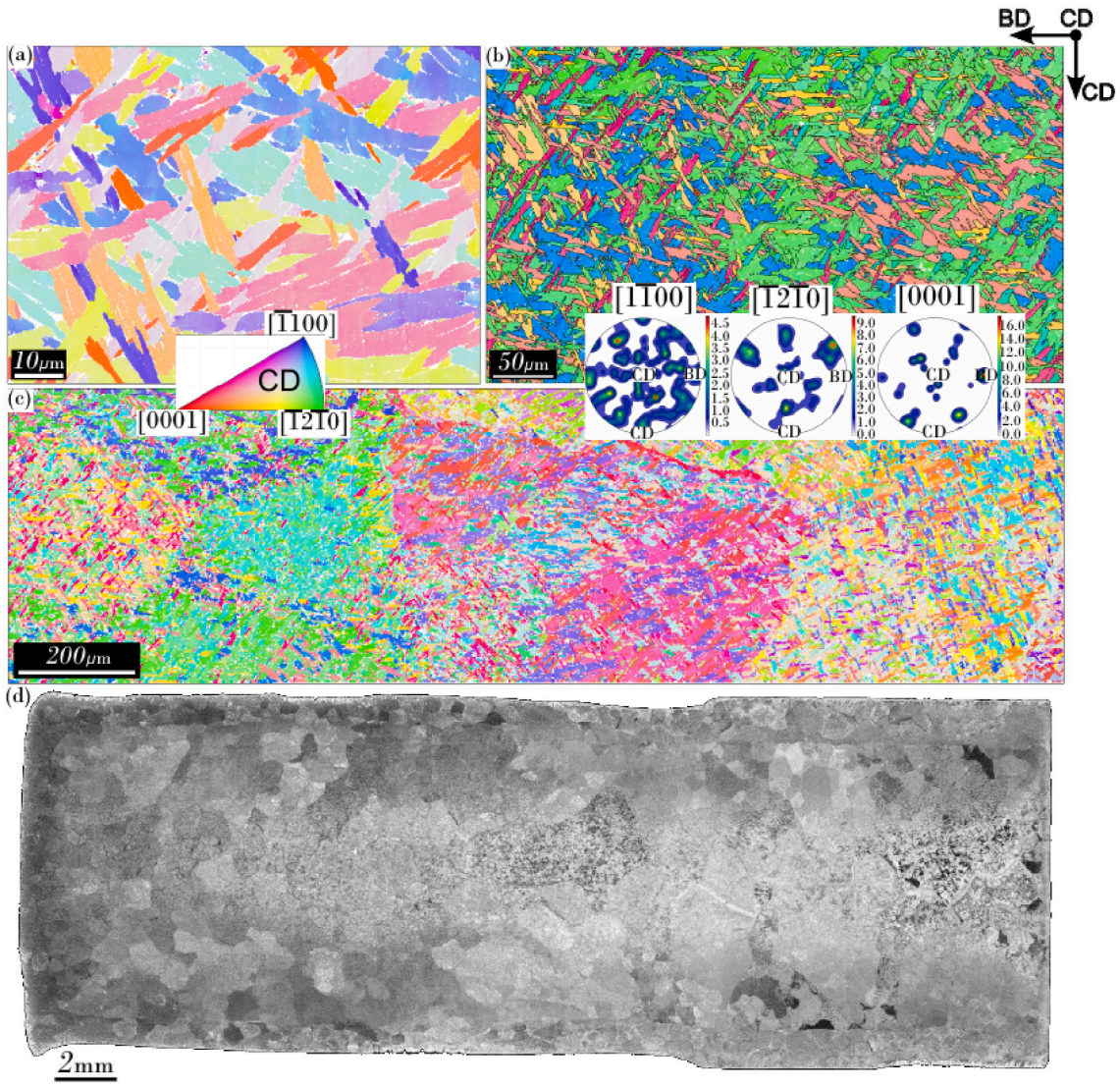

Fig. 10. EBSD IPF-CD (out-of-page) maps for Specimen SP11, which underwent 2-stage cogging operations (below and above β-transus), including (a)97.5 × 66.6, (b) 487.2 × 334.8 and, (c)1826.0 × 504.0 μm map sizes all within the cogged zone, also showing pole figures that demonstrate no clear texture (c). IPF-CD (out-of-page) key is the same for all EBSD images. (d) Light macrograph of Specimen SP11 showing the macro-structure of martensite towards the specimen edges with a central Widmanstätten (basketweave) structure.

strain rate is not a limitation of the present equipment or method. Higher bites per minute, and strain rates can be explored in future studies with the employment of the apparatus with various load frames, similar to the study by Niu et al. [60] where the strain rate of $0.01s^{-1}$ was used, but trials at up to $1s^{-1}$ have also been demonstrated.

The influence of prior-β processing on the evolution of microstructure during α + β forging was examined by Lahiri et al. [61] Air cooling the heat-treated β phase resulted in lamellar structures with a homogeneous morphology and distribution of crystallographic orientations. However, deformation above the β-transus temperature led to the formation of elongated β grains, which affected the nucleation and growth of the α-phase during cooling [61,53]. Consequently, this alteration modified the morphology and orientation distribution of the lamellae and had an impact on the globularisation process. The presence of shorter and non-randomly oriented lamellae within the deformed prior-β grains led to higher rates of spheroidisation. Additionally, the direction of α + β forging in relation to β upsetting was found to be significant, as seen evidenced in Zhao et al.'s work [53]. It was observed in Zhao et al.'s work that higher rates of globularisation were achieved when two perpendicular directions were applied. This method could be applied to examine these phenomena closely with low cost.

Dyja et al. [62] studied the optimal angles of tilt in cogging through FEM and a series of upsetting and cogging trials. Another strength of this new set-up is that it could be directly applied to validating and optimising compression angles such as these. This inclusion of micro-upsetting with the apparatus, alongside micro-cogging, could be a major benefit of the apparatus that can lead to an overall increase in future material and open-die forging schedule optimisation studies. Similarly, in Zhang et al.'s [22] work a similar style of 60% upsetting between 90° rotations was employed for the multi-directional isothermal forging, the new set-up method will allow for the geometry of the forged components to be more akin to those in industrial ingot-to-billet conversion.

β-Processing cogging is an important stage of the thermomechanical processing of Ti-6Al-4V. More specifically, reducing the β grain size from the coarse as-cast structure is a critical process requirement. Fig. 14 presents fixed bin width histograms from an example dataset (*i.e.,* AHT, SP1, SP7, and SP11) of how the presented set-up can be used to study the control and measurement of β grain size reduction. It can be observed from Fig. 14, that the mean β grain equivalent circular diameter

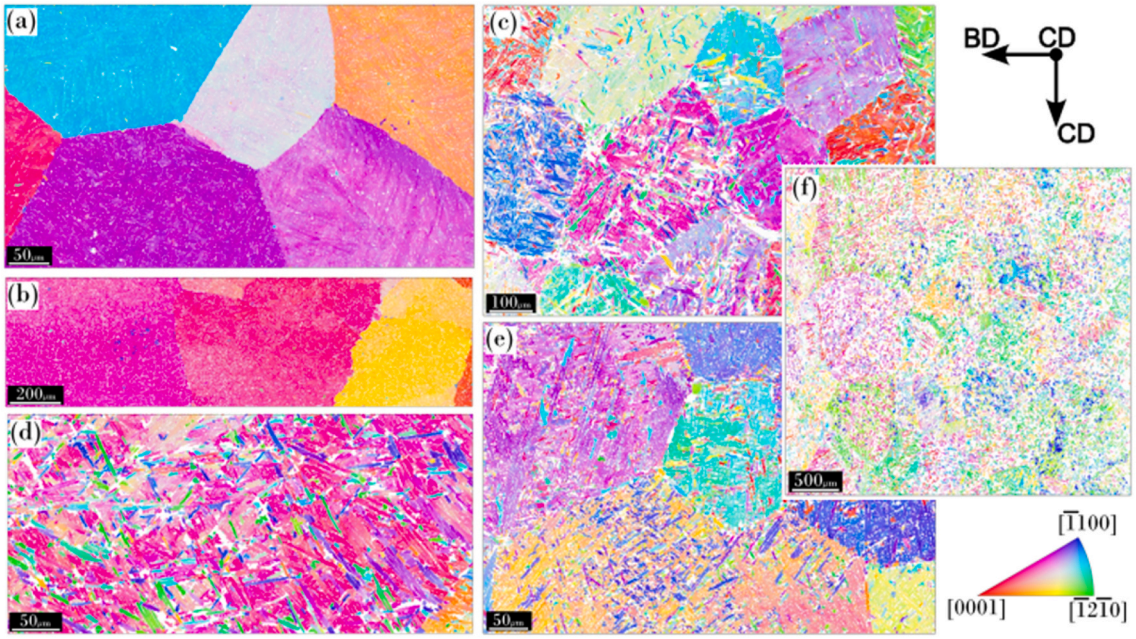

Fig. 11. Parent β grain reconstruction (PBGR) obtained from EBSD map data of (a) the AHT material, (b) Specimen SP11, (cogged to 13.1% cross-section reduction) above β-transus, (c) Specimen SP5 (cogged to 8.1% cross-section reduction) at 950 °C, (d) Specimen SP6 (cogged to 10.8% cross-section reduction) at 950 °C, (e) Specimen SP9 (7.3% cross-section reduction) to an octagonal geometry at 950 °C and, (f) Specimen SP7 (12.2% cross-section reduction) at 950 °C. IPF-CD (out-of-page) key is the same for all maps.

decreased from 0.58 mm in the AHT material to 0.45 mm and 0.39 mm in Specimens SP1 and SP7 respectively. The mean β grain equivalent circular diameter in Specimen SP11, presented in Fig. 14(d) increased to 0.61 mm, this was influenced by the large Widmanstätten grain structure in the centre of the specimen, implying that the specific temperature and overall time at temperature allowed for significant diffusion within the test specimen.

During cogging processes, it is often necessary to conduct reheating steps to maintain the desired temperature distribution throughout the specimen. In the studies reviewed, short reheating times were used due to the small size of the specimens. For instance, Ari-Gur and Semiatin [63] and Kim et al. [64] used annealing times of 3 min and 10 min respectively between forging steps. Although these short annealing times had minimal impact on the microstructure, a slight grain coarsening was observed after multiple deformation and reheating cycles [64]. However, in industrial cogging operations, the reheating time for a billet is significantly longer, often lasting several hours. This prolonged reheating period has the potential to induce microstructural changes that can influence subsequent process steps. Nevertheless, these potential effects have not been thoroughly investigated. Cooling rates from temperatures above the β-transus can also have an overall effect on the level of globularisation that can be achieved after α + β processing. Due to the isothermal nature of the present study, the reheating of the component was not investigated, but could play a role in future work using the described apparatus and methodology.

One outcome from this work is the small-scale reproducibility and inexpensive set-up that could be easily standardised and used in materials testing labs across the globe to accelerate data capture and understanding of materials evolution. This study has aimed to prove the applicability of this new method at a higher temperature and demonstrate the potential research value for forged materials of high commercial interest. Design iteration for further improvement of this method could yield highly beneficial rewards for materials engineers, due to the higher test rates and lower cost of materials and energy that facilitates the testing of larger batches and simultaneous exploration of more process parameters (degrees of freedom).

Another advantage that small-scale open-die forging can offer is the ability to target the study of specific microstructural phenomena. As an example, this study showed that the cogging of small samples using the described new apparatus, with increments of 5% deformation was successful in inducing globularisation in Ti-6Al-4V material with lamellar initial microstructure. The specimens displayed an increasing level of microstructural transformation with deformation increments. Mechanisms of globularisation at high temperature involve the formation of α/α boundaries within the prior laths due to localised shear and buckling, and continuous dynamic recrystallisation. These are followed by the penetration of beta phase along these α/α boundaries ultimately leading to fragmentation of α laths into smaller globular grains [47, 65–69]. The progressive breaking up of α laths into smaller grains with increasing deformation (Fig. 9), observed in the present study, agrees with these mechanisms.

Globularisation kinetics are known to be dependent on the processing route and strain path [70–72]; and slower kinetics have been observed during multi-axial forging compared to uniaxial compression trials [73,74]. However, the mechanisms of microstructural evolution related to the strain path during cogging are not well understood. The described new apparatus was successfully used to introduce some level of globularisation (28%) in a small-scale Ti-6Al-4V sample via a cogging schedule; and it can be utilised to further explore the effect of process parameters such as strain increment and angle between deformation directions on globularisation.

The present study has been able to map, in part, the dependence of the degree of globularisation on the amount of plastic strain imparted to the specimens. The experimental data points do seem to align to the initial rising curve of a JMAK-type sigmoid (S-shape). Further studies could be carried out to verify whether the material behaves according to the JMAK model, whereby higher levels of strain should be investigated. The effect of total strain is difficult to separate from the temporal component however, as to achieve larger deformations more bites are required with the present setup, which in turn takes more time at temperature to complete. *I.e.* We have not been able to achieve large single-bite deformations at the chosen strain rates. If α globularisation can be modelled as a dynamic recrystallisation (DRX) process, then some formulation of JMAK equation with suitable values of material

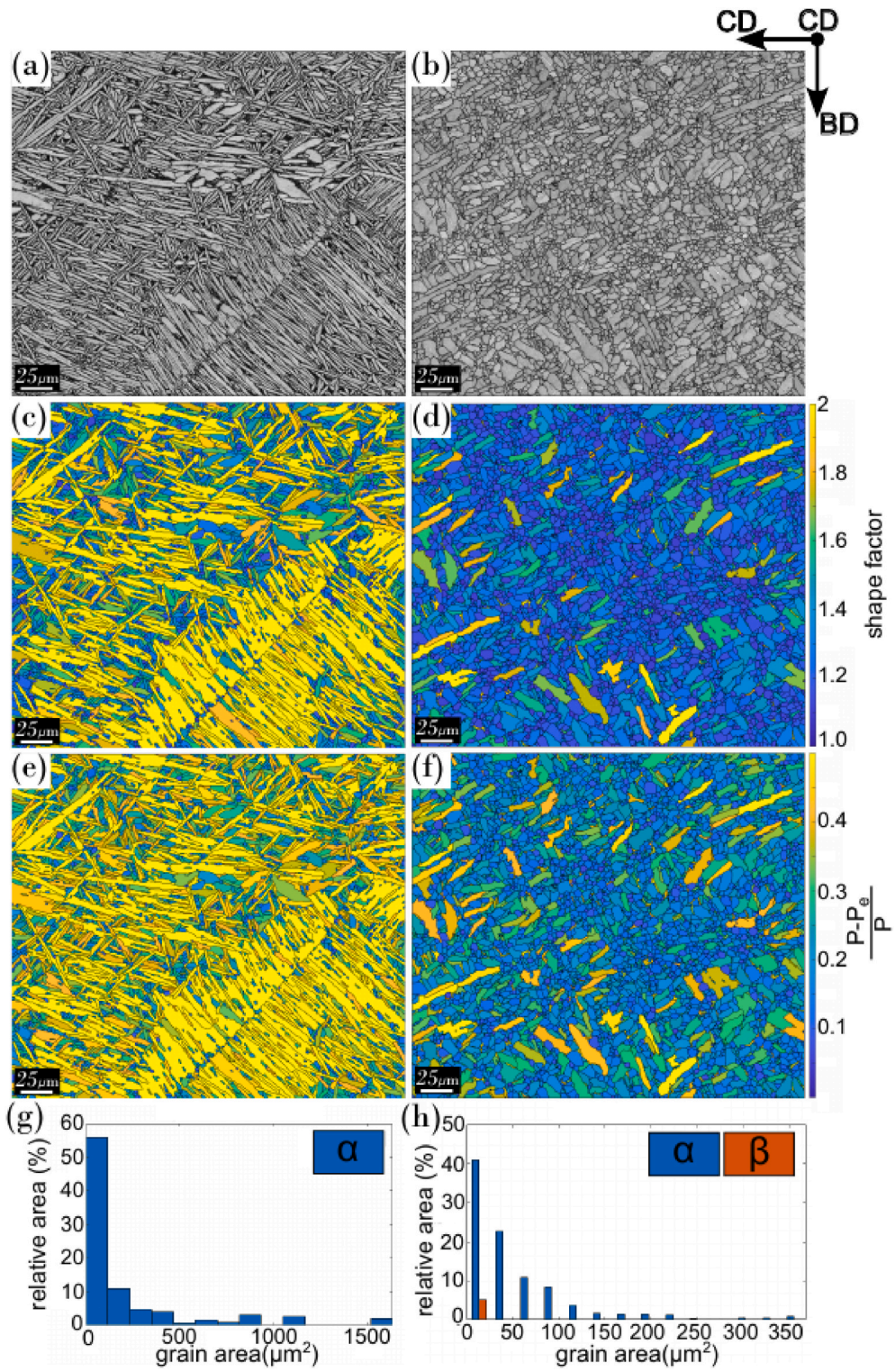

Fig. 12. Processed EBSD data output from cogged zones of: **LEFT** Specimen SP2 (2.3% cross-section reduction) in comparison with **RIGHT** Specimen SP7 (12.2% cross-section reduction), (a)–(b) band contrast images with grain boundaries, (c)–(d) shape factor plots, (e)–(f) plots of the relative difference between the perimeter and equivalent perimeter and, (g)–(h) plots of grain size distributions. Calculated and visualised using the MTEX Toolbox in MATLAB®.

Table 4
Geometric material constants for the dislocation density model.

K_1	K_2	K_3	K_4	Q_s	Q_z	Q_b	m	n	β_1	β_2	λ_1	q
4.1×10^8	410	0.1	0.01	27,500	150,000	150,000	0.833	1	0.324	4.5×10^{13}	0.0398	1.168

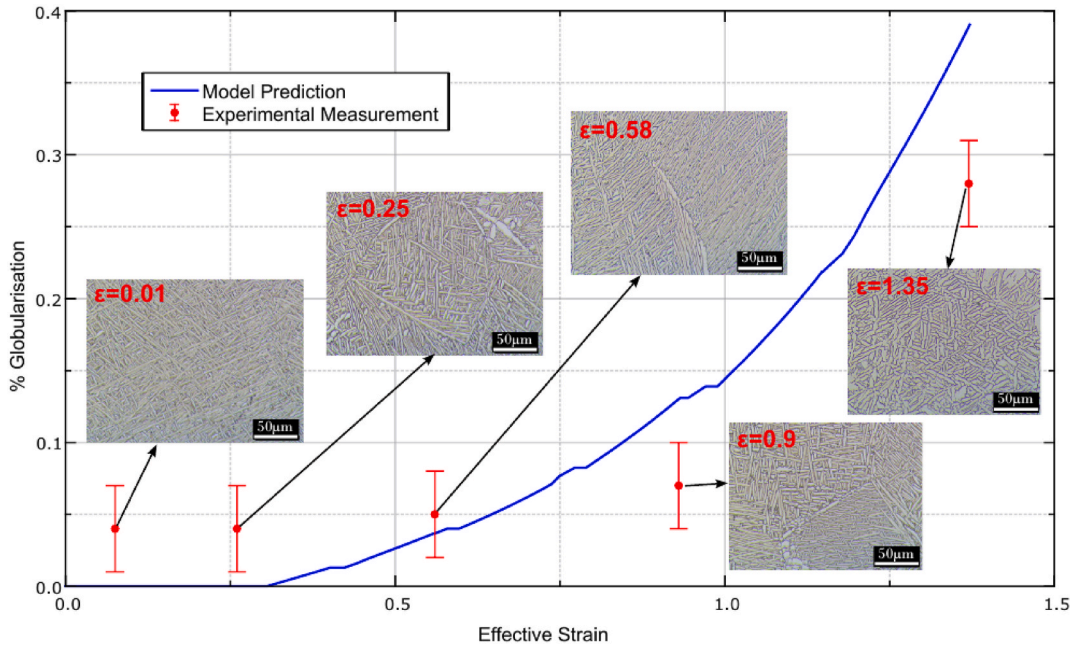

Fig. 13. Predicted and experimental globularised fractions for Specimens SP1 to SP7.

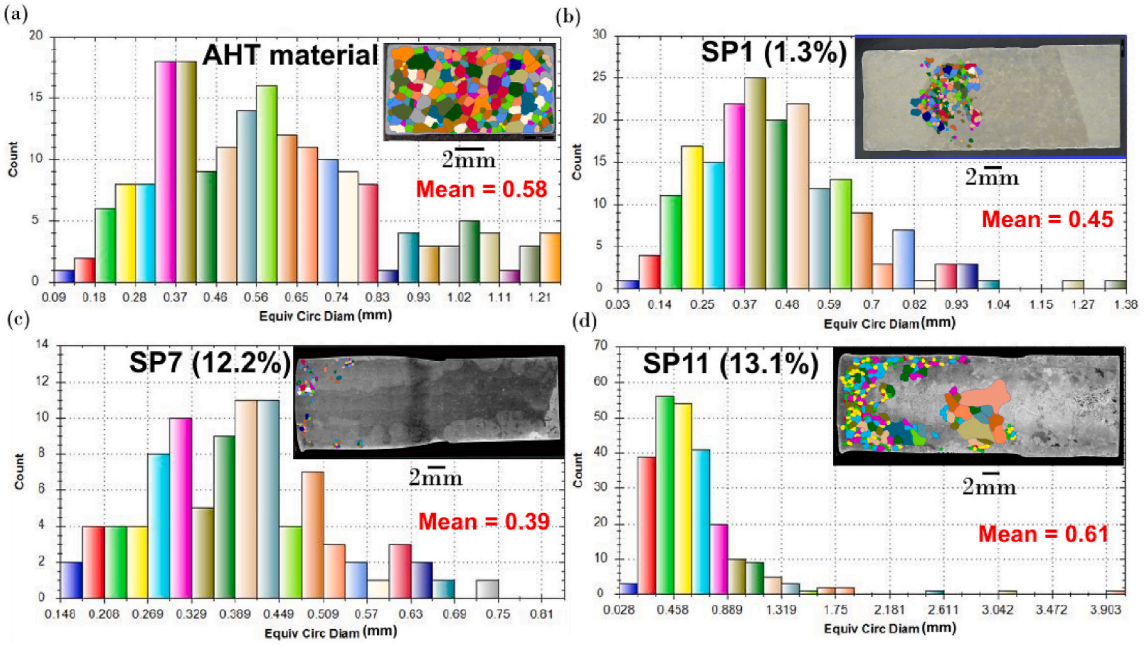

Fig. 14. Collection of histograms with fixed bin width presenting grain count against equivalent circular diameter, captured from a representative area/cogged zone of: (a) AHT material, (b) Specimen SP1 (1.3%), (c) Specimen SP7 (12.2%), and (d) Specimen SP11.

parameters could be used to explain the experimentally observed behaviour. With accompanying temperature and strain-rate dependent models of the flow stress behaviour, FE modelling could be used to map spatially the extent of globularisation across forgings. Such an approach has been demonstrated successfully for DRX in single and dual phase alloy forgings by Razali and Joun [75], and Joun et al. [76]. The models described by the authors could certainly apply to DRX during super-transus forging, but may need adjustment to the overall formulation for sub-transus deformation due to increased microstructural complexity and large number of active slip systems.

The discrepancies in results between the current globularisation model prediction and experimental measurements can be due to model calibration and any differences in strain distribution between these two scales. However, the trend indicates that microstructural changes observed at a small-scale (from experimentation) in this work correlate with those experienced at a larger scale (from Fabris' model [57]), and that the described apparatus can help accelerate research thanks to its increased throughput of testing, and lower material requirement. Additionally, it proves the new apparatus presented in this work may be used for calibration of future material models, where the user can capitalise on the advantages of scaled down experimentation.

Another research avenue would be the study of macrozones in $\alpha + \beta$ titanium alloys. Macrozones in $\alpha + \beta$ titanium are millimetre long clusters of α grains with nearly, or the same, crystallographic orientation

[77]. These macrozones are known to have a negative effect on the fatigue performance of the alloy. What remains unknown with these features is how to sufficiently break them down on an industrial scale, owing to the large primary β grain size. Huang et al.'s work [78] investigated the formation and evolution of macrozones in Ti–6242S alloy during TMP and found that the formation of macrozones is related to the evolution of primary α (*i.e.,* α_p) and β grains. The new set-up presented in this work would allow for further understanding of macrozone evolution using less material.

However, with the novelty of the set-up, some design challenges remain for high temperature testing (*i.e.,* ≥950 °C). Firstly, the isothermal conditions and repeat passes progressively remove lubricant from the sample during the experiments. This increases the risk and likelihood that the test-specimen will stick to the dies for longer test runs that require larger numbers of bites. This problem is exacerbated when the starting mini-billet geometry is rectilinear rather than cylindrical. Possible solutions could include a high-temperature lubricant delivery system or the use of highly sintered ceramic dies.

Another consideration would be the "flying-blind" nature of the current method at higher forging temperatures (>600 °C) using split tube furnaces. Lower temperature tests on copper and aluminium alloys used an environmental chamber, which had an observation window that facilitated convenient monitoring of the specimen position and its in-situ adjustment. An improved set up could feature a high-temperature viewport or fibre-optic imaging of the specimen position.

Tribology is another important consideration. The tool operating life is crucial in bulk metal forming which can be affected by many factors in the system including the machine, tool, and workpiece [79]. Hot forging dies are subjected to a range of cyclic thermal, mechanical, chemical, and tribological loads. Various parameters during hot forging including the friction and lubrication conditions can influence the final billet geometry and microstructure. For these tests a combination of a glass coating and boron nitride lubricant was used, which due to the isothermal conditions was found to have an increased sticking effect as the number of bites increased. It was found as part of a following study using specimens with square starting cross-sections, that both a higher cross-section reduction in a single bite as well as the increased surface area, influenced this sticking factor. Short checks had to be introduced to ensure that the specimens were free from die sticking before rotation.

This study provides positive evidence that the presented laboratory equipment can be used to study open die forging/cogging of commercial alloys which are of high research interest. The desired capability of hot forging of titanium alloys informed the experiment design decisions: the load frame capacity, specimen size with respect to available furnace volume, and the choice and geometry of the tooling materials. Overall, this study has acted as a reinforcement that miniaturised cogging can be used to inform upstream to more costly intermediate and larger research scale testing and help provide data for development of microstructure-sensitive CPFE models, which could be used to advance digital-twin development for the next generation of data-driven metallurgical manufacturing.

5. Conclusions

This study has investigated the capability of a new laboratory-scale apparatus in the open-die forging/cogging of Ti-6Al-4V alloy below and above the transus temperature in an effort to simulate ingot-to-billet conversion of material for high-value component manufacturing. The following conclusions can be derived.

1. The experimental apparatus and testing methodology were successfully applied to forging of a dual-phase aerospace titanium alloy. Various stages of microstructural evolution in Ti-6Al-4V have been successfully captured through precise control of multi-directional compressive deformation.
2. FE modelling has been used to evaluate the stress-state and plastic strain within the forged specimens, demonstrating apparatus capability for data generation in future advanced digital-twin development. The simulated forgings matched well the 3D geometries and cross-section reductions measured from the test specimens using GOM scans.
3. The small scale multi-directional open die forging (cogging) experiments have demonstrated the ability to achieve globularisation of the α phase in Ti-6Al-4V. Manual analyses and EBSD data processing have shown the degree of globularisation to depend on the overall level of plastic strain sustained by the specimens. This is consistent with existing understanding of the phenomenon and its mechanisms. JMAK type behaviour is evident in the experimental data, but would need further experimental verification.
4. Some correlation has been observed between the evolution of α-globularisation captured from the new experimental technique and an α-globularisation model calibrated from larger-scale forging trials. Further calibration of the model parameters could improve the overall match of the model with the experimental data trend.
5. In contrast to our original pilot study using the miniature cogging apparatus, an increased temperature capability has been successfully validated. There is good potential for applying the described equipment and techniques to the study of materials with even higher temperature capabilities, such as namely superalloys, if some of the outlined limitations are overcome and tooling materials are upgraded.
6. The experimental approach combined with complementary simulations and larger scale experiments could be instrumental in the development of future digital twins for open die forging, which could enable data-driven real-time process optimisation in industry.

CRediT authorship contribution statement

David Connolly: Methodology, Validation, Formal analysis, Investigation, Data curation, Writing – original draft, Visualization. **Mathieu Fabris:** Writing – review & editing, Validation, Formal analysis. **Giribaskar Sivaswamy:** Supervision, Writing – review & editing. **Salaheddin Rahimi:** Conceptualization, Supervision, Writing – review & editing. **Vassili Vorontsov:** Conceptualization, Supervision, Project administration, Writing – review & editing.

Declaration of competing interest

The authors declare that they have no known competing financial interests or personal relationships that could have appeared to influence the work reported in this paper.

Acknowledgements

The authors would like to acknowledge the support provided by the Advanced Forming Research Centre (AFRC), University of Strathclyde, which receives partial funding from the UK's High Value Manufacturing CATAPULT. VAV would also like to acknowledge funding support from the University of Strathclyde under the Chancellor's Fellowship scheme. DJC and VAV also thank Dr. Vivian Tong, Mr. Tony Fry, and Dr. Ken Mingard (National Physical Laboratory) for valuable training and consultation, and Sebastien Nouveau (Aubert & Duval) for constructive discussion that led to this study.

References

[1] Welsch G, Boyer R, Collings EW. Materials properties handbook: titanium alloys. ASM International; 1993.
[2] Donachie MJ. Titanium: a technical guide. ASM international; 2000. https://doi.org/10.31399/asm.tb.ttg2.9781627082693.

[3] Semiatin SL. An overview of the thermomechanical processing of/β titanium alloys: current status and future research opportunities. Metall Mater Trans 2020;51(6):2593–625. https://doi.org/10.1007/s11661-020-05625-3.

[4] Lütjering G, Williams JC. Titanium matrix composites. Springer; 2007. https://doi.org/10.1007/978-3-540-73036-1_9.

[5] Weston NS, Jackson M. FAST-forge - a new cost-effective hybrid processing route for consolidating titanium powder into near net shape forged components. J Mater Process Technol 2017;243:335–46. https://doi.org/10.1016/j.jmatprotec.2016.12.013.

[6] Liu S, Shin YC. Additive manufacturing of Ti6Al4V alloy: a review. Mater Des 2019;164:107552. https://doi.org/10.1016/j.matdes.2018.107552.

[7] Herzog D, Seyda V, Wycisk E, Emmelmann C. Additive manufacturing of metals. Acta Mater 2016;117:371–92. https://doi.org/10.1016/j.actamat.2016.07.019.

[8] Huang R, Riddle M, Graziano D, Warren J, Das S, Nimbalkar S, Cresko J, Masanet E. Energy and emissions saving potential of additive manufacturing: the case of lightweight aircraft components. J Clean Prod 2016;135:1559–70. https://doi.org/10.1016/J.JCLEPRO.2015.04.109.

[9] Kritzinger W, Karner M, Traar G, Henjes J, Sihn W. Digital Twin in manufacturing: a categorical literature review and classification. IFAC-PapersOnLine 2018;51(11):1016–22. https://doi.org/10.1016/j.ifacol.2018.08.474.

[10] Roters F, Eisenlohr P, Hantcherli L, Tjahjanto DD, Bieler TR, Raabe D. Overview of constitutive laws, kinematics, homogenization and multiscale methods in crystal plasticity finite-element modeling: theory, experiments, applications. Acta Mater 2010;58(4):1152–211. https://doi.org/10.1016/j.actamat.2009.10.058.

[11] Pérez M, Dumont C, Nodin O, Nouveau S. Impact of forging direction on the recrystallization behaviour of nickel base superalloy AD730 billet material at subsolvus temperatures. Mater Char 2018;146:169–81. https://doi.org/10.1016/j.matchar.2018.10.003.

[12] Souza PM, Sivaswamy G, Bradley L, Barrow A, Rahimi S. An innovative constitutive material model for predicting high temperature flow behaviour of inconel 625 alloy. J Mater Sci 2022;57(44):20794–814. https://doi.org/10.1007/s10853-022-07906-1.

[13] Souza PM, Sivaswamy G, Hall L, Rahimi S. An analysis of the forgeability of Ti-10V-2Fe-3Al β titanium alloy using a combined estrin mecking and avrami material constitutive model. Int J Mech Sci 2022;216:106975. https://doi.org/10.1016/j.ijmecsci.2021.106975.

[14] ASTM. Standard practice for compression tests of metallic materials at elevated temperatures with conventional or rapid heating rates and strain rates. 2018. https://doi.org/10.1520/E0209-18.

[15] Cho JR, Park CY, Yang DY. Investigation of the cogging process by three-dimensional thermo-viscoplastic finite element analysis. Proc IME B J Eng Manufact 1992;206(4):277–86. https://doi.org/10.1243/PIME_PROC_1992_206_084_02.

[16] Kukuryk M. Numerical analysis of strains and stresses in the hot cogging process. Journal of Applied Mathematics and Computational Mechanics 2018;17:45–52. https://doi.org/10.17512/jamcm.2018.3.04.

[17] Kang G, Lee K, Lee S. Computer simulation of microstructure evolution during hot forging of waspaloy. In: Proceedings of the Korean society for technology of plasticity conference, the Korean society for technology of plasticity; 2007. p. 53–6.

[18] Bai Q, Lin J-g, Dean TA, Balint DS, Gao T, Zhang Z. Modelling of dominant softening mechanisms for Ti-6Al-4V in steady state hot forming conditions. Mater Sci Eng, A 2013;559:352–8. https://doi.org/10.1016/j.msea.2012.08.110.

[19] Ding R, Guo ZX, Wilson A. Microstructural evolution of a Ti-6Al-4V alloy during thermomechanical processing. Mater Sci Eng, A 2002;327(2):233–45. https://doi.org/10.1016/S0921-5093(01)01531-3.

[20] Coyne-Grell A, Blaizot J, Rahimi S, Violatos I, Nouveau S, Dumont C, Nicolaÿ A, Bozzolo N. Recrystallization mechanisms and associated microstructure evolution during billet conversion of a gamma-gamma' nickel based superalloy. J Alloys Compd 2022;916:165465. https://doi.org/10.1016/j.jallcom.2022.165465.

[21] Coyne-Grell A, Blaizot J, Rahimi S, Violatos I, Nouveau S, Dumont C, Nicolaÿ A, Bozzolo N. Evolution of γ' precipitation during the early stages of industrial forging of a nickel-based superalloy. Metall Mater Trans A 2023;54(5). https://doi.org/10.1007/s11661-022-06878-w.

[22] Zhang ZX, Qu SJ, Feng AH, Shen J. Achieving grain refinement and enhanced mechanical properties in Ti-6Al-4V alloy produced by multidirectional isothermal forging. Mater Sci Eng, A 2017;692:127–38. https://doi.org/10.1016/j.msea.2017.03.024.

[23] Ward M. Metal forming and forging – finding a new place within high value manufacturing through advanced, industrial scale research. Ironmak Steelmak 2015;42(4):252–8. https://doi.org/10.1179/0301923314Z.000000000347.

[24] Rahimi S, Violatos I, Wynne B, Jackson M. Digital twins for high-value components. Mater World 2022;30(6):38–41. https://www.iom3.org/resource/digital-twins-for-high-value-components.html.

[25] Blackwell PL. From materials characterisation to pre-production validation: from materials characterisation to pre-production validations to providing processing solutions to industry. In: International conference on new forming technology, CHN; 2015. https://doi.org/10.1051/matecconf/20152101004.

[26] Lutering G, Williams JG. Titanium. Berlin, Heidelberg: Springer-Verlag; 2003.

[27] Connolly D, Sivaswamy G, Rahimi S, Vorontsov V. Miniaturised experimental simulation of open-die forging. J Mater Res Technol 2023;26:3146–61. https://doi.org/10.1016/j.jmrt.2023.08.073.

[28] Semiatin S, Seetharaman V, Weiss I. Flow behavior and globularization kinetics during hot working of Ti-6Al-4V with a colony alpha microstructure. Mater Sci Eng, A 1999;263(2):257–71. https://doi.org/10.1016/S0921-5093(98)01156-3.

[29] Souza PM, Sivaswamy G, Andreu A, Rahimi S. A novel cyclic thermal treatment for enhanced globularisation kinetics in Ti-6Al-4V alloy: experimental, constitutive and FE based analyses. J Alloys Compd 2022;898:162859. https://doi.org/10.1016/j.jallcom.2021.162859.

[30] Sabban R, Bahl S, Chatterjee K, Suwas S. Globularization using heat treatment in additively manufactured Ti-6Al-4V for high strength and toughness. Acta Mater 2019;162:239–54. https://doi.org/10.1016/j.actamat.2018.09.064.

[31] Zhang J, Li H, Zhan M. Review on globularization of titanium alloy with lamellar colony. Manuf Rev 2020;7:18. https://doi.org/10.1051/mfreview/2020015.

[32] M. O. Bodunrin, L. H. Chown, J. W. van der Merwe, K. K. Alaneme, Hot working of Ti-6Al-4V with a complex initial microstructure, International Journal of Material Forming (2018) Hot working of Ti-6Al-4V with a complex initial microstructure .. doi.org/10.1007/s12289-018-1457-9.

[33] Kim D-H, Lee C-M. Experimental investigation on machinability of titanium alloy by laser-assisted end milling. Metals 2021;11:1552. https://doi.org/10.3390/met11101552.

[34] Taylor GI, Quinney H. The latent energy remaining in a metal after cold working. Proceedings of the Royal Society of London. Series A Containing Papers of a Mathematical and Physical Character 1934;143(849):307–26. https://doi.org/10.1098/rspa.1934.0004.

[35] Kulakov M, Rahimi S, Semiatin SL. Effect of deformation heating on microstructure evolution during hot forging of Ti-6Al-4V. Metall Mater Trans 2022;53(2):407–19. https://doi.org/10.1007/s11661-021-06493-1.

[36] Rittel D, Zhang LH, Osovski S. The dependence of the Taylor-Quinney coefficient on the dynamic loading mode. J Mech Phys Solid 2017;107:96–114.

[37] Charles HMM, Lieou KC, Bronkhorst CA. Strain localization and dynamic recrystallization in polycrystalline metals: thermodynamic theory and simulation framework. Int J Plast 2019;119:171–87. https://doi.org/10.1016/j.ijplas.2019.03.005.

[38] Soares GC, Hokka M. The Taylor-Quinney coefficients and strain hardening of commercially pure titanium, iron, copper, and tin in high rate compression. Int J Impact Eng 2021;156:103940. https://doi.org/10.1016/j.ijimpeng.2021.103940.

[39] Abrams H. Grain size measurement by the intercept method. Metallography 1971;4(1):59–78. https://doi.org/10.1016/0026-0800\%2871\%2990005-X.

[40] Thorvaldsen A. The intercept method - 2. Determination of spatial grain size. Acta Mater 1997;45(2):595–600. https://doi.org/10.1016/S1359-6454(96)00198-X.

[41] Bachmann F, Hielscher R, Schaeben H. Grain detection from 2d and 3d EBSD data - specification of the MTEX algorithm. Ultramicroscopy 2011;111(12):1720–33. https://doi.org/10.1016/j.ultramic.2011.08.002.

[42] I. O. for Standardization (ISO). Metallic materials: Vickers hardness test 2018. https://doi.org/10.3403/BSENISO6507. ISO 6507-1:2018.

[43] Semiatin L, editor. Open-die forging, metalworking: bulk forming. ASM International; 2005. book/chapter-pdf/497191/a0003978.pdf.

[44] Shell E, Semiatin S. Effect of initial microstructure on plastic flow and dynamic globularization during hot working of Ti-6Al-4V. Metall Mater Trans 1999;A. https://doi.org/10.1007/S11661-999-0232-4.

[45] Bignon M, Bertrand E, del Castillo PEJR-D, Tancret F. Martensite formation in titanium alloys: crystallographic and compositional effects. J Alloys Compd 2021;872:159636. https://doi.org/10.1016/j.jallcom.2021.159636.

[46] Tong V, Joseph S, Ackerman A, Dye D, Britton T. Using transmission Kikuchi diffraction to characterise α variants in an α + β titanium alloy. J Microsc 2017;267. https://doi.org/10.1111/jmi.12569.

[47] Stefansson N, Semiatin SL. Mechanisms of globularization of Ti-6Al-4V during static heat treatment. Metall Mater Trans 2003;34(3):691–8. https://doi.org/10.1007/s11661-003-0103-3.

[48] Semiatin S, Stefansson N, Doherty R. Prediction of the kinetics of static globularisation of Ti-6Al-4V. Metall Mater Trans 2005;36:1372–6. https://doi.org/10.1007/s11661-005-0229-6.

[49] Song H-W, Zhang S-H, Cheng M. Dynamic globularization kinetics during hot working of a two phase titanium alloy with a colony alpha microstructure. J Alloys Compd 2009;480(2):922–7. https://doi.org/10.1016/j.jallcom.2009.02.059.

[50] xuan Wang K, dong Zeng W, qing Zhao Y, tao Shao Y, gang Zhou Y. Prediction of dynamic globularization of Ti-17 titanium alloy with initial lamellar microstructure during hot compression. Mater Sci Eng, A 2010;527(23):6193–9. https://doi.org/10.1016/j.msea.2010.06.059.

[51] Ma X, Zeng W, Tian F, Zhou Y. The kinetics of dynamic globularization during hot working of a two phase titanium alloy with starting lamellar microstructure. Mater Sci Eng, A 2012;548:6–11. https://doi.org/10.1016/j.msea.2012.03.022.

[52] Wang K, Zeng W, Zhao Y, Lai Y, Zhou Y. Dynamic globularization kinetics during hot working of ti-17 alloy with initial lamellar microstructure. Mater Sci Eng, A 2010;527(10):2559–66. https://doi.org/10.1016/j.msea.2010.01.034.

[53] Zhao AM, Yang H, Fan XG, Gao PF, Zuo R, Meng M. The flow behavior and microstructure evolution during (α + β) deformation of β wrought TA15 titanium alloy. Mater Des 2016;109:112–22. https://doi.org/10.1016/j.matdes.2016.07.001.

[54] Babu B, Lindgren L-E. Dislocation density based model for plastic deformation and globularization of Ti-6Al-4V. Int J Plast 2013;50:94–108. https://doi.org/10.1016/j.ijplas.2013.04.003.

[55] Gao P, Yang H, Fan X, Zhu S. Unified modeling of flow softening and globularization for hot working of two-phase titanium alloy with a lamellar colony microstructure. J Alloys Compd 2014;600:78–83. https://doi.org/10.1016/j.jallcom.2014.02.110.

[56] Sun Z, Yang H, Han G, Fan X. A numerical model based on internal-state-variable method for the microstructure evolution during hot-working process of TA15 titanium alloy. Mater Sci Eng, A 2010;527(15):3464–71. https://doi.org/10.1016/j.msea.2010.02.009.

[57] Fabris M. Evolution of globularisation in Ti-6Al-4V alloy during secondary cogging operations under industrial scale conditions. University of Strathclyde; 2022. https://books.google.co.uk/books?id=6p9bzwEACAAJ.
[58] Ouyang D, Cui X, Lan X, Wan X, Pan L. Experimental study and numerical simulation of lamellar globularization for TC21 titanium alloy during multidirectional forging. Mater Res Express 2022;9(8). https://doi.org/10.1088/2053-1591/ac743c.
[59] Jin Y, Zhang Y, Zhao G, Li W. Kinetics and crystallography of globularization in the additively manufactured Ti-6Al-4V. Results in Engineering 2023;18:101140. https://doi.org/10.1016/j.rineng.2023.101140.
[60] Niu L, Zhang Q, Wang B, Han B, Li H, Mei T. A modified Hansel-Spittel constitutive equation of Ti-6Al-4V during cogging process. J Alloys Compd 2022;894:162387. https://doi.org/10.1016/j.jallcom.2021.162387.
[61] Lahiri I, (Mondal) DL, Bhargava S. Effect of prior β processing on superplasticity of (α + β) thermomechanically treated Ti-6Al-4V alloy. Mater Manuf Process 2003;18(4):621–35. https://doi.org/10.1081/AMP-120022501. arXiv:.
[62] Dyja H, Tukibay AA, Mashekov SA. The influence of technological conditions of the process of cogging in flat dies on the quality of two-phase titanium alloys. Arch Metall Mater 2016;61(2A):671–6. https://doi.org/10.1515/amm-2016-0114.
[63] Ari-Gur P, Semiatin SL. Evolution of microstructure, macrotexture and microtexture during hot rolling of Ti-6Al-4V. Mater Sci Eng, A 1998;257(1):118–27. https://doi.org/10.1016/S0921-5093(98)00829-6.
[64] Kim J, Park K-T, Shim I, Hong S. Globularization behavior of ELI grade Ti6Al4V alloy during non-isothermal multi-step forging. Materials Transactions - MATER TRANS 2008;49:215–23. https://doi.org/10.2320/matertrans.MER2007224.
[65] Weiss I, Froes FH, Eylon D, Welsch GE. Modification of alpha morphology in Ti-6Al-4V by thermomechanical processing. Metall Trans A 1986;17(11):1935–47. https://doi.org/10.1007/BF02644991.
[66] Mironov S, Murzinova M, Zherebtsov S, Salishchev GA, Semiatin SL. Microstructure evolution during warm working of Ti-6Al-4V with a colony-α microstructure. Acta Mater 2009;57(8):2470–81. https://doi.org/10.1016/j.actamat.2009.02.016.
[67] Li C, Zhang X-y, Zhou K-c, Peng C. Relationship between lamellar α evolution and flow behavior during isothermal deformation of Ti-5Al-5Mo-5V-1Cr-1Fe near β titanium alloy. Mater Sci Eng, A 2012;558:668–74. https://doi.org/10.1016/j.msea.2012.08.074.
[68] Furuhara T, Poorganji B, Abe H, Maki T. Dynamic recovery and recrystallization in titanium alloys by hot deformation. Jom 2007;59:64–7. https://doi.org/10.1007/s11837-007-0013-8.
[69] Zherebtsov S, Murzinova M, Salishchev G, Semiatin SL. Spheroidization of the lamellar microstructure in Ti-6Al-4V alloy during warm deformation and annealing. Acta Mater 2011;59(10):4138–50. https://doi.org/10.1016/j.actamat.2011.03.037.
[70] Muszka K, Lopez-Pedrosa M, Raszka K, Thomas M, Rainforth W, Wynne B. The impact of strain reversal on microstructure evolution and orientation relationships in Ti-6Al-4V with an initial alpha colony microstructure. Metall Mater Trans 2014;45. https://doi.org/10.1007/s11661-014-2590-9.
[71] Enikeev CP V Korshunov A, Mazurski FU, Salishchev MI, Dmitriev GA, Muravlev A V OV. Grain-structure refinement in titanium alloy under different loading schedules. J Mater Sci 1996. https://doi.org/10.3390/met12030454.
[72] Fan X, Zheng H, Zhang Y, Zhang Z, Gao P, Zhan M, Liu J. Acceleration of globularization during interrupted compression of a two-phase titanium alloy. Mater Sci Eng, A 2018;720:214–24. https://doi.org/10.1016/j.msea.2018.02.026.
[73] Kedia B, Balasundar I, Raghu T. Globularisation of alpha lamellae in titanium alloy: effect of strain, strain path and starting microstructure. Trans Indian Inst Met 2018;71. https://doi.org/10.1007/s12666-018-1323-y.
[74] Sheed D, Kashyap B, Singh R. Study of globularization in ti-6al-4v alloy during non-isothermal multiple forging and annealing. In: Proceedings of 22nd TheIIER international conference; 2015. 978-93-82702-97-9.
[75] Razali MK, Joun MS. A new approach of predicting dynamic recrystallization using directly a flow stress model and its application to medium Mn steel. JMR&T 2021:1881–94. https://doi.org/10.1016/j.jmrt.2021.02.026.
[76] Joun MS, Razali MK, Chung SH, Irani M. A direct method of calculating flow-related dynamic recrystallization parameters for generality and accuracy in predicting microstructural evolution. JMR&T 2022:3894–907. https://doi.org/10.1016/j.jmrt.2022.04.060.
[77] Nait-Ali A, Hémery S, Gueguen M. How macrozone size and morphology influence yield in titanium alloys investigated using fast Fourier transform-based crystal plasticity simulations. Int J Solid Struct 2021;216:1–16. https://doi.org/10.1016/j.ijsolstr.2021.01.008.
[78] Huang L, Sun Z, Cao J, Yin Z. The formation and evolution of macrozone in Ti-6242S alloy during thermo-mechanical processing. J Alloys Compd 2021;861:158533. https://doi.org/10.1016/j.jallcom.2020.158533.
[79] Behrens B-A, Bouguecha A, Lüken I, Mielke J, Bistron M. 5.11 - tribology in hot forging, comprehensive materials processing. Oxford: Elsevier; 2014. p. 211–34. https://doi.org/10.1016/B978-0-08-096532-1.00538-0.